ANL/ESD/11-3

Computational Mechanics Research and Support for Aerodynamics and Hydraulics at TFHRC

Year 1 Quarter 2 Progress Report

Energy Systems Division

About Argonne National Laboratory

Argonne is a U.S. Department of Energy laboratory managed by UChicago Argonne, LLC under contract DE-AC02-06CH11357. The Laboratory's main facility is outside Chicago, at 9700 South Cass Avenue, Argonne, Illinois 60439. For information about Argonne and its pioneering science and technology programs, see www.anl.gov.

Availability of This Report

This report is available, at no cost, at http://www.osti.gov/bridge. It is also available on paper to the U.S. Department of Energy and its contractors, for a processing fee, from:

U.S. Department of Energy
Office of Scientific and Technical Information
P.O. Box 62
Oak Ridge, TN 37831-0062
phone (865) 576-8401
fax (865) 576-5728
reports@adonis.osti.gov

ANL/ESD/11-2

Computational Mechanics Research and Support for Aerodynamics and Hydraulics at TFHRC

Year 1 Quarter 2 Progress Report

by
S.A. Lottes, R.F. Kulak,and C. Bojanowski
Center for Transportation Research
Energy Systems Division, Argonne National Laboratory

April 2011

Argonne NATIONAL LABORATORY

Computational Mechanics Research and Support for Aerodynamics and Hydraulics at **TFHRC**

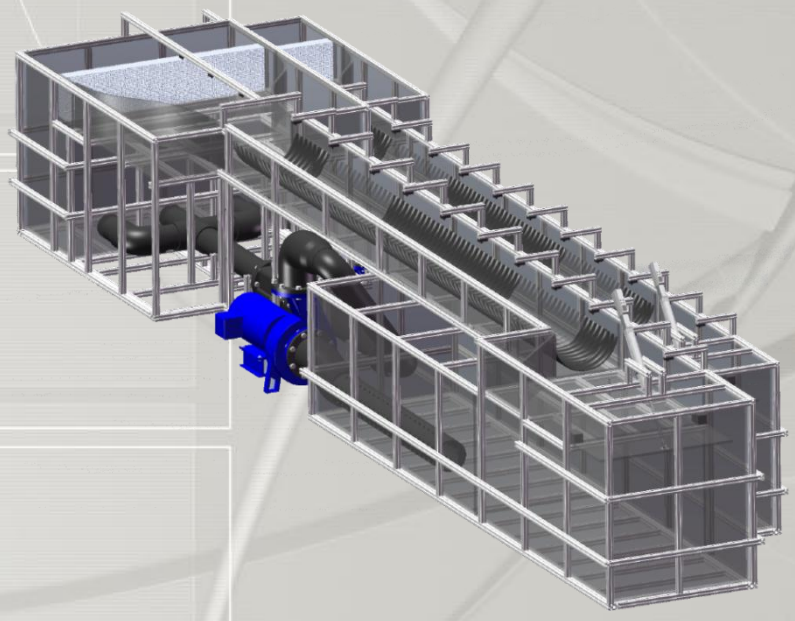

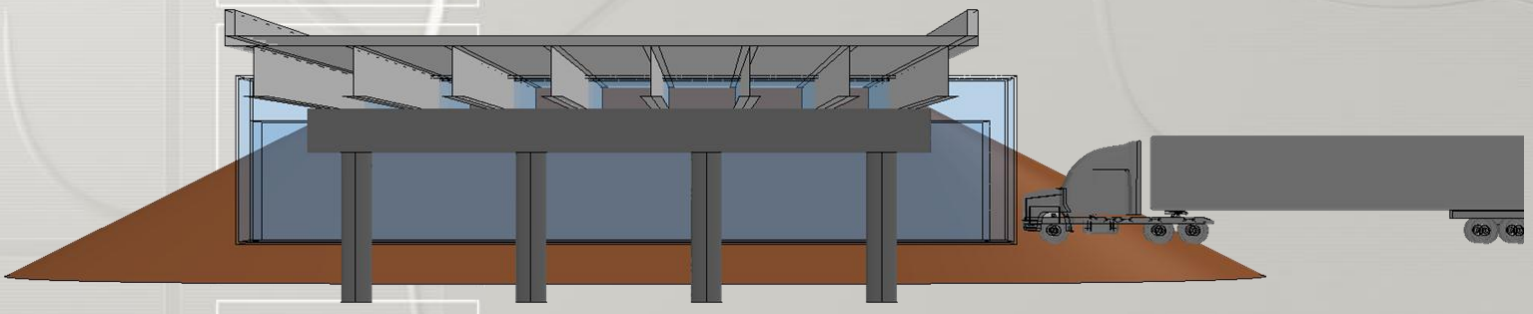

Quarterly Report

January through March 2011

Y1Q2

Computational Mechanics Research and Support for Aerodynamics and Hydraulics at TFHRC
Year 1 Quarter 2 Progress Report

Energy Systems Division (ES)
Argonne National Laboratory (ANL)

Principal Investigators:
Steven A. Lottes, Ph.D.

Ronald F Kulak, Ph.D., PE, FASME

Contributor:
Cezary Bojanowski, Ph.D.

Submitted to:
Federal Highway Administration

Kornel Kerenyi, Ph.D.
Turner-Fairbank Highway Research Center
Federal Highway Administration
6300 Georgetown Pike
McLean, VA 22101

Harold Bosch, Ph.D.
Turner-Fairbank Highway Research Center
Federal Highway Administration
6300 Georgetown Pike
McLean, VA 22101

April, 2011

Table of Contents

List of Figures

List of Tables

1. Introduction and Objectives

This project was established with a new interagency agreement between the Department of Energy and the Department of Transportation to provide collaborative research, development, and benchmarking of advanced three-dimensional computational mechanics analysis methods to the aerodynamics and hydraulics laboratories at the Turner-Fairbank Highway Research Center for a period of five years, beginning in October 2010. The analysis methods employ well-benchmarked and supported commercial computational mechanics software. Computational mechanics encompasses the areas of Computational Fluid Dynamics (CFD), Computational Wind Engineering (CWE), Computational Structural Mechanics (CSM), and Computational Multiphysics Mechanics (CMM) applied in Fluid-Structure Interaction (FSI) problems.

The major areas of focus of the project are wind and water loads on bridges — superstructure, deck, cables, and substructure (including soil), primarily during storms and flood events — and the risks that these loads pose to structural failure. For flood events at bridges, another major focus of the work is assessment of the risk to bridges caused by scour of stream and riverbed material away from the foundations of a bridge. Other areas of current research include modeling of flow through culverts to assess them for fish passage, modeling of the salt spray transport into bridge girders to address suitability of using weathering steel in bridges, vehicle stability under high wind loading, and the use of electromagnetic shock absorbers to improve vehicle stability under high wind conditions.

This quarterly report documents technical progress on the project tasks for the period of January through March 2011.

1.1. Computational Fluid Dynamics Summary

The primary Computational Fluid Dynamics (CFD) activities during the quarter concentrated on the development of models and methods needed to complete the next steps in scour and culvert modeling. Several new students have begun work on these projects as part of their work in their degree programs. Training materials and new tutorials for a STAR-CCM+ training course were developed that focused on the techniques needed to address current research problems in CFD model development and analysis. The new materials and tutorials were used in a STAR-CCM+ training course held on March 30 and 31,

2011. The course had 25 participants including the new students, engineers from TFHRC, two professors, and variety of other people with an interest in CFD analysis applied to hydraulics and wind engineering problems.

Work on improving models that use mesh morphing to handle grid motion for an arbitrarily moving boundary, which is the case in scour modeling, has continued for the transient pressure flow scour modeling effort. In transient scour modeling, effort focused on developing and testing entrainment rate functions. Obtaining a reasonably accurate entrainment rate function that is general and can be applied at any point on an eroding bed using the local conditions is key to achieving a transient scour modeling capability. Few entrainment functions appear in the literature because entrainment rate experiments are very difficult to control and there is often a large amount of uncertainty in the experimental data. As a consequence both the functional form and the fitting parameters are difficult to obtain. An approach that uses transient scour hole depth data from experiment and quasi-steady CFD simulation of the measured bed contour to obtain the transient change in bed shear to fit parameters of candidate entrainment functions is being pursued.

Culvert analysis focused on determination of detailed velocity distributions to improve design procedures for culverts that need to allow for fish passage. A work plan for culvert experiments and CFD analysis of culverts to assess fish passage capability for various low flow conditions was developed at TFHRC. The plan includes analysis of many sets of conditions in large culverts that are too large for laboratory testing. CFD analysis and experiments are being used for the analysis of a small diameter culvert section that will fit in the laboratory. CFD analysis alone will be used for assessing fish passage capability for large scale culverts. Full 3D multiphase CFD analysis of long culvert barrel sections would consume too many computational resources and take too long to complete the project within the planned timeframe. A CFD approach that applies cyclic boundary conditions with single phase water flow yields a much smaller model geometry that can be analyzed on the TRACC cluster within an hour or two. With this approach a large number of parametric cases can be analyzed over a period of a few weeks. Work on this methodology has shown that it works well for a small scale culvert.

1.2. Computational Multiphysics Mechanics Summary

Computational multiphysics mechanics research continued in several areas. Research focused on developing robust models for treating the fluid-structure interaction that occurs as a semi-trailer truck travels under a bridge and forces the mixture of air and salt spray onto the weathering steel. Based on blueprints provided by TFHRC of the Bridge No. 4172 in West Virginia, an initial multiphysics model was developed to represent a large semi-trailer truck traveling through air under the bridge. Simulations were performed to develop robust modeling techniques.

TRACC staff and NIU staff (professor/student) started working on two Wind Engineering projects. The first project deals with the effects of wind loading on vehicles and the second is the development of an electromagnetic shock absorber control algorithm that can increase the stability of trucks driving over bridges in high wind conditions.

Turner Fairbank Highway Research Center is performing erosion tests on cohesive soils under different flow conditions. A terse overview of standard tests performed for characterizing soil was presented. The tests are performed to (1) to determine parameters used in constitutive models and (2) to define the failure surface. The constitutive models would be applicable to slope stability of the soil around scour holes. Other test may need to be performed to characterize quantities relevant to erosion mechanics, and this will be researched further.

2. Computational Fluid Dynamics

The effort during the second quarter was concentrated on developing an approach to obtaining a good sediment entrainment rate function for pressure flow scour, development of methods for enhanced analysis of culvert flow for fish passage that account for the velocity distribution over a cross section, and preparation of training material for a CFD training course that was conducted at TRACC on March 30-31, 2011.

2.1. Entrainment Functions for RANS Scour Models and Tests of Alternatives

Entrainment function by Van Rijn and a chemical kinetic rate law analogy proposed by Lottes [1] have been considered, and initial testing of these model functions for clear water pressure flow scour was done. The Van Rijn is a power law function of the form:

$$E_b = A_0 \left(\frac{\tau}{\tau_c} - 1\right)^n \quad for\ \tau > \tau_c \tag{2.1}$$

$$E_b = 0 \quad for\ \tau < \tau_c \tag{2.2}$$

Where E_b is the sediment pickup rate in units of mass per unit sediment bed area and per unit time, kg/(m^2 s). The rate law is proposed by Lottes [1] and has the form:

$$E_b = A_0 \left(\frac{\tau}{\tau_c}\right)^n \exp\left(-\frac{A_1\,\tau_c}{\tau}\right) \tag{2.3}$$

where A_0, A_1, and n are fitting parameters.

Experiments were conducted at TFHRC to better identify the critical velocity and critical shear stress in an open flume with no bridge deck obstruction. The sediment pick up rates and equivalently the bed recession rates for a range mean flow velocities were measured. The range of mean velocities was limited by the difficulties of collecting all of the sand and measuring small bed depth changes at low flow

and erosion conditions. Experimental conditions were limited at high erosion rates because the flume was not designed for live bed scour. The CFD software STAR-CCM+ was used to obtain the mean bed shear stress in the test section for these experiments. The data were then organized to yield the bed recession rate as a function of the mean bed shear stress. Van Rijn's rate law using the published constants, an adjusted constant and Lottes's [1] proposed law were compared to the data as shown in Figure 2.1. The figure shows how the entrainment functions behave in the range of the experimental data. The power law form of the Van Rijn function does not appear to have the correct curvature in the range of the data. It also goes to zero at the critical shear stress, where in reality some entrainment occurs below the mean critical shear stress value because turbulent fluctuations occasionally exert sufficient force on the particles in the bed to move them at a rate that goes asymptotically to zero as the mean shear approaches zero. The kinetic law entrainment function appears to match measurements relatively well in the range of the data and has the property that it drops smoothly to very low entrainment rates below the critical shear stress.

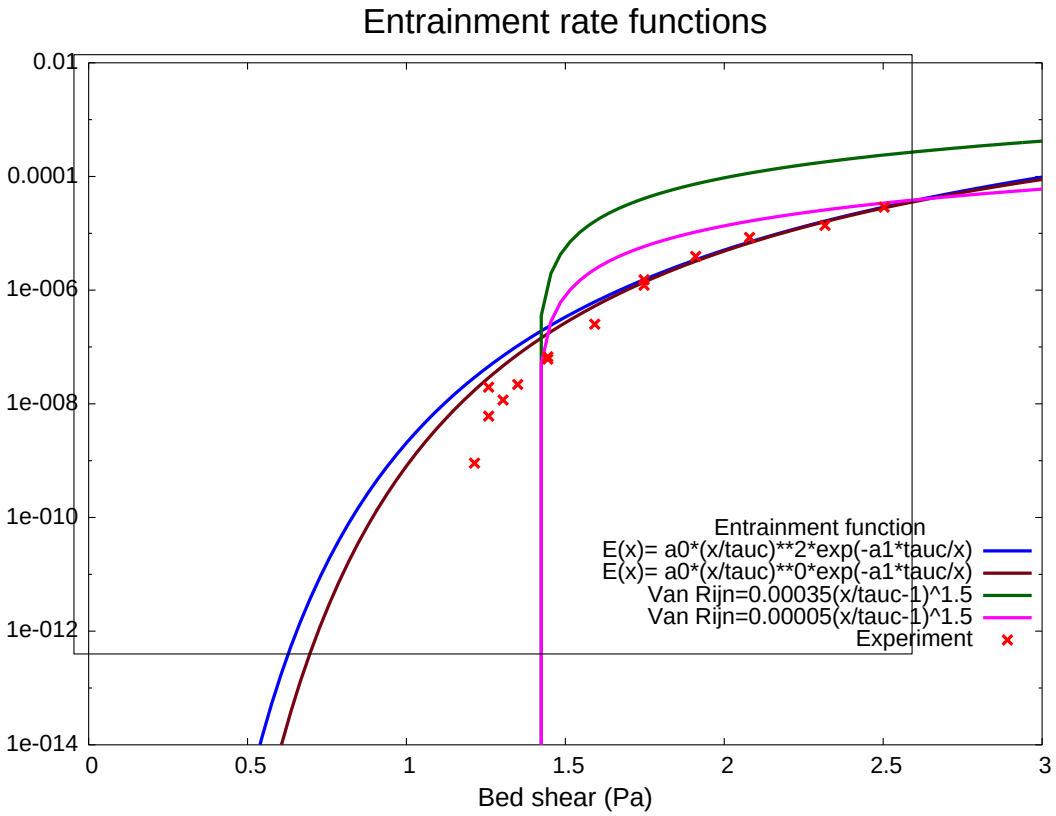

Figure 2.1: Entrainment rate functions

These entrainment functions were tested using STAR-CCM+ in a 2D model of pressure flow scour under a flooded bridge deck, and the removal rate of material in these tests was much too fast. The erosion rate and bed shear stress under a flooded bridge deck when the deck is first submerged in the flume flow is large and outside the range of data from unobstructed flow scour experiments. A task to obtain

more accurate entrainment functions by using data from one of the transient pressure flow scour experiments conducted at TFHRC to fit entrainment rate function constants has been started.

One problem in using the data from a transient pressure flow scour experiment to fit the entrainment rate functions is that although the bed scour depth is known over time, the shear stress is not known. Use of CFD analysis to obtain the needed bed shear stress at the times when bed depth measurements were taken during the scour experiments is planned. At any particular time the flow is nearly steady (quasi-steady) on the erosion time scale, and therefore, the shear stress distribution is determined by the partially scoured bed contour at a given time. Guo [2] developed a function form to fit the data from these experiments.

$$Y = \left[1 - e^{-\frac{T}{T_c}}\right]^{\frac{1}{4}} \qquad 2.4$$

Where $Y = y/y_s$ and $T = tV_u/h_b$ and T_c is a fitting parameter. The depth at 42 hours is assumed to be 99% of the asymptotic depth, giving a value of y_s = 3.42 cm for the case with the initial bridge height above the bed, h_b, equal to 16 cm. The upstream mean velocity is V_u = 0.515 m/s, and the mean sand diameter is d_{50} = 2.18 mm. The maximum scour depth equation then becomes:

$$y = y\_s\left[1 - e^{-\frac{T}{T_c}}\right]^{\frac{1}{4}} \qquad 2.5$$

Guo's fit [2] yields $T_c = 1.56 \times 10^5$ while Lottes [1] obtained 1.90153×10^5 using gnuplot. This relation is shown in Figure 2.2. Both of the fitting constants are likely within the range of experimental uncertainty. The constant obtained using the regression feature of gnuplot has a smaller slope in the early period and a slightly greater slope near the end time.

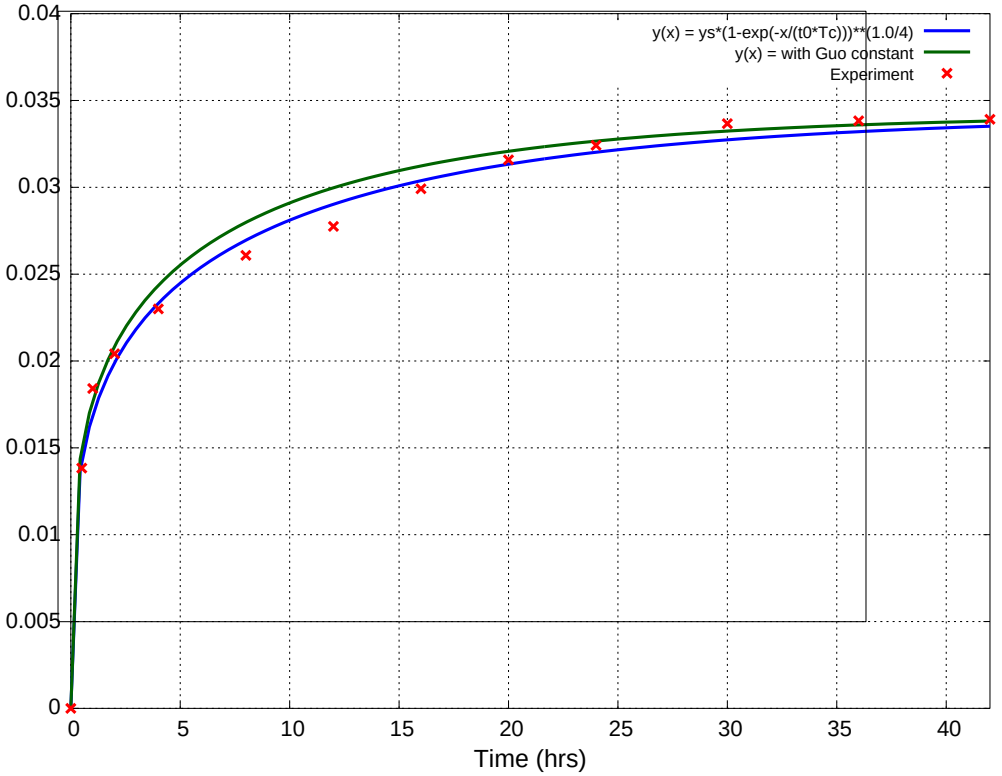

Figure 2.2: Maximum depth versus time (h_b = 16)

2.2. Test Mesh Morphing Applied to Clear Water Pressure Flow Scour

The scour rate can be obtained by differentiating Equation 2.5. Then the shear stress at the point of maximum scour can be computed from quasi-steady conditions and the scour bed profile at a series of times from 0 to 42 hours, and the entrainment rate function constants can be fit to match the data.

Work on obtaining the needed shear stress data was carried out assuming that the scour bed profiles are similar to the final profile with the maximum depth varying as a function of time.

Guo [3] empirically derived the pressure-flow scour profiles under the TFHRC six-girder test bridge deck as:

$$\frac{y}{y_s} = -exp\left(-\left|\frac{x}{W}\right|^{2.5}\right) \; for\; the\; region\; upstream \qquad 2.6$$

and

$$\frac{y}{y_s} = -1.055exp\left(-\frac{1}{2}\left|\frac{x}{W}\right|^{1.8}\right) + 0.055 \; for \; the \; region \; downstream \qquad 2.7$$

where y is the depth at location x on the bed, y_s is maximum depth of scour, and W is bridge width.

Equations 2.6 and 2.7 are assumed to give the two dimensional bed profile at time t if y_s .is taken to be the maximum scour depth at time t. The mesh morphing feature of STAR-CCM+ was used to increase the maximum depth of the profile from zero to the final depth at 42 hours and the shear stress profiles along the bed were computed. The sequence of bed profiles is shown in Figure 2.3.

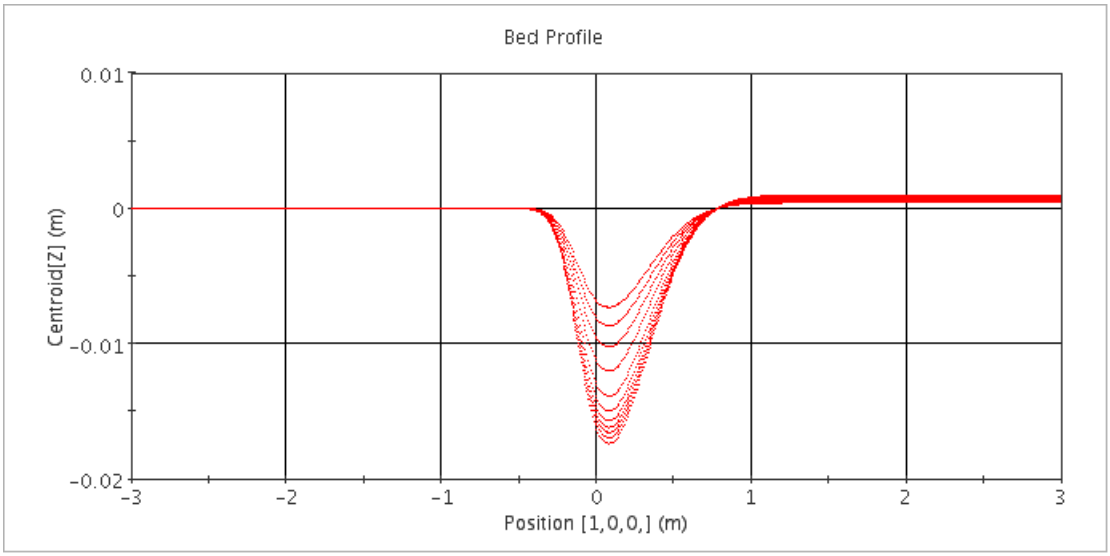

Figure 2.3: Bed morphing with time

2.2.1. References

1. Lottes, S.A., *Hydraulics and Scour Modeling Notes*, unpublished, Argonne National Laboratory, 2010.
2. Guo, Junke, *Time-dependent scour of submerged bridge flows*, paper in preparation, Department of Civil Engineering University of Nebraska-Lincoln, 2011.
3. Guo, Junke, et.al., *Bridge Pressure Flow Scour at Clear Water Threshold Condition*, Trans. Tianjin Univ., 2009, 15;079-094.

2.3. Computational Modeling and Analysis of Flow through Large Culverts for Fish Passage

Fish passage through culverts is an important component of road and stream crossing design. As water runoff volume increases, the flow often actively degrades waterways at culverts and may interrupt

natural fish migration. Culverts are fixed structures that do not change with changing streams and may instead become barriers to fish movement. The most common physical characteristics that create barriers to fish passage include excessive water velocity, insufficient water depth and large outlet drop heights, turbulence within the culvert, and accumulation of sediment and debris. Major hydraulic criteria influencing fish passage are: flow rates during fish migration periods, fish species, roughness, and the length and slope of the culvert.

The objective of this work is to develop approaches to CFD modeling of culvert flows and to use the models to perform analysis to assess flow regions for fish passage under a variety of flow conditions. The flow conditions to be tested with CFD analysis are defined in the tables of a work plan from Turner Fairbank Highway Research Center (TFHRC) [6]. The CFD models are being verified by comparing with data from experiments conducted at the TFHRC. A primary goal of CFD analysis of culverts for fish passage is to determine the local cross section velocities and flow distributions in corrugated culverts under varying flow conditions. In order to evaluate the ability of fish to traverse corrugated metal culverts, the local average velocity in vertical strips from the region adjacent to the culvert wall where it is slow out to the centerline where it is fast under low flow conditions will be determined.

The work covered is this report includes initial work to identify CFD modeling techniques that can be used to complete the large number of tests in the TFHRC work plan over a period of a few months. Using a full 3D model of a flume with culvert or a long full size culvert barrel with inlet and outlet geometry is very computationally expensive and can require more than a week to complete one test using the multiphase flow VOF model. A modeling approach that uses a short section of culvert geometry and assumes fully developed flow conditions is being developed. In this method, cyclic boundary conditions are applied to compute the fully developed flow condition using a small 3D geometry. Free surface flow using the VOF model cannot be used with this method. Use of the cyclic boundary condition requires an assumption of a nearly flat free surface that can be modeled with a symmetric boundary condition that allows a free slip water velocity at that boundary. With this approach several test cases can be completed per day. Part of the verification of the model approach includes a comparison of the single phase model with the VOF multiphase model in a long section of culvert.

A number of researchers are now investigating approaches to using CFD to assess fish passage. Blank et.al [1], formulated an approach that quantifies the three-dimensional velocity field within the culvert barrel using a CFD model with two-phase model for air and water to model the free-surface using ANSYS-CFX. It tests the use of hydrodynamic modeling to assess potential culvert barriers to upstream fish movement using an algorithm that estimates energy paths and passage along those paths taking into account the swimming speed and fatigue time relationship for fish within the velocity field. Muste et.al [2] conducted steady and unsteady flow laboratory measurements for a variety of culvert-barrel cross-section shapes and configurations. Real time data for discharge and water levels at several upstream and downstream locations of a culvert structure were collected. Khan [3] developed a 3-D CFD model of a vertical-slot fishway to characterize fishway hydrodynamics. Model results indicated a strong 3-D velocity field in the fishway, with eddies, flow separations and vortices. Velocities and drag forces encountered by upstream migrating fish and energy expenditures in ascending the fishway are

determined from the fishway hydrodynamics. A quantified study on energy expenditure in the fishways was developed to optimize the design, operation, and management of fishways. Gardner [4] determined the maximum swimming speed that can be sustained by a certain species of fish for a period of ten minutes. The fish were collected by electrofishing from local streams. After resting for a certain time, the fish were placed in a flume and allowed to accommodate at a resting velocity. The velocity was then increased by a certain amount for a fixed time interval, while returning to the resting velocity. A Microsoft Excel model was created based on the results. The model uses the critical velocities as guidelines for maximum flow rates in the hydrologic design of culverts. In the previous phase of this project, Vishnu Vardhan Reddy Pati [5], developed a 3D two-phase (water-air) VOF simulation model to study the flow development through the culverts. The study estimates the flow losses for different corrugation sizes. Evaluation and comparison of the friction head losses and the corresponding slopes based on different methods were conducted.

2.3.1. Model of Culvert Section with Fully Developed Flow Using Cyclic Boundary Conditions

In this study a simulation model is developed using the commercial CFD software STAR-CCM+. A small section of the culvert barrel is modeled with cyclic boundaries at the inlet and outlet sections of the computational domain. The cyclic boundary approach shortens the simulation time required to establish a fully developed flow field with a known mass flow rate. This approach greatly reduces the amount of computational resources and computation time needed to analyze the flow field. For simplicity the culvert model considered in this study is a symmetric quarter of the culvert section with corrugations from trough to 2nd trough as shown in Figure 2.4. Sensitivity of the solution was tested with 5 variations of the mesh, including two base sizes and 3 combination of refinement in the region with the corrugations where recirculation zones develop. The refinement is defined by specifying a reduction of mesh size for volume within an annulus intersecting the model as shown in Figure 2.5.

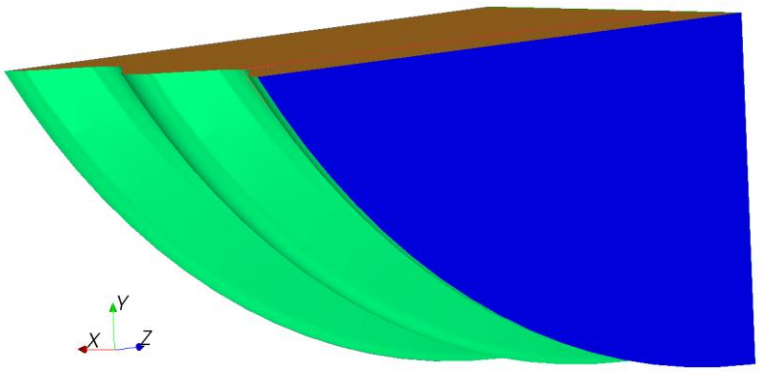

Figure 2.4: Symmetric center trough to trough culvert section geometry

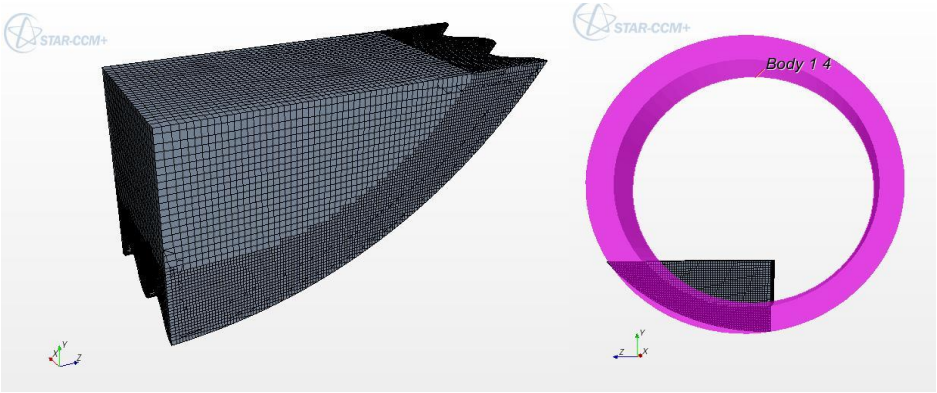

Figure 2.5: Example hexahedral mesh refined in volume of pink annulus

The computational model is based on the three-dimensional transient RANS k-epsilon turbulence model with wall function treatment. A fully developed flow condition is generally reached after flow through a relative long entrance length of corrugated barrel section. Computing the developing flow in order to get the fully developed flow can be avoided by using cyclic boundary conditions. Cyclic boundary conditions are set at the inlet and outlet planes of the computational domain to produce a periodic fully developed flow with a known mass flow rate. In order to create the cyclic boundary with a fully developed flow condition, all outlet variables are mapped back to the inlet interface, except for the pressure because there is a pressure drop corresponding to the energy losses in the culvert section. The pressure drop requires a "pressure jump" between outlet and inlet cyclic interface. When the mass flow rate is specified, the pressure jump needed to balance the pressure drop for the specified mass flow is iteratively computed by the CFD software as part of the solution process.

Boundary conditions for the model are listed in Table 2.1. The procedure to create the cyclic boundaries requires creation of a model object that associates the inlet and outlet boundaries at the cyclic boundary interface. The cyclic interface is defined with a fully developed flow property with a specified mass flow rate.

Table 2.1: Boundary conditions

Boundary	Name	Type
Face at minimum x value	Inlet	Cyclic boundary condition
Face at maximum x value	Outlet	Cyclic boundary condition
Water surface	Top	Symmetry plane
Centerline	Center	Symmetry plane
all other surfaces	Barrel	No-slip wall

2.3.2. Mesh Refinement Study

A mesh refinement study was conducted to identify mesh sizes that will be suitable for parametric study of the culvert conditions in the work plan. This initial study focused only on the 36 inch diameter culvert. Sensitivity to mesh refinement will need to be checked for the larger culverts in the work plan when the geometry for those culverts is built. Volumetric controls in an annular volume covering the corrugated wall region are used to create a finer mesh in that region in order to get a better resolution of the flow field with recirculation zones between the corrugations. Meshing also includes a prism layer consisting of orthogonal prismatic cells along the wall boundaries.

A volumetric control was created around the corrugated section of the barrel to specifically refine the mesh further around this region with respect to the base. Table 2.2 shows four of the five different mesh size distributions that were tested. A coarser version of mesh 2 is not shown. While meshes 1 and 2 use a uniform mesh size distribution with a mesh size of 10 mm and 5 mm respectively, mesh types 3-5 use volume controls for meshing to achieve a finer mesh with increased number of cells near the corrugated wall region to better resolve the recirculation zones in this region.

Table 2.2: Comparison of Tested Mesh Refinements

Case	Base size (m)	%Refinement in Corrugation Zone	Cells in Mesh	Mass Residual	% Deviation in Cross Section Mass Flow
Mesh 1	0.010	None	9,325	4.5×10^{-3}	0.379
Mesh 2	0.005	None	82,337	2.9×10^{-8}	0.057
Mesh 3	0.010	40	167,254	1.4×10^{-6}	0.023
Mesh 4	0.010	20	825,924	1.0×10^{-6}	0.011
Mesh 5	0.005	40	959,829	1.9×10^{-6}	0.011

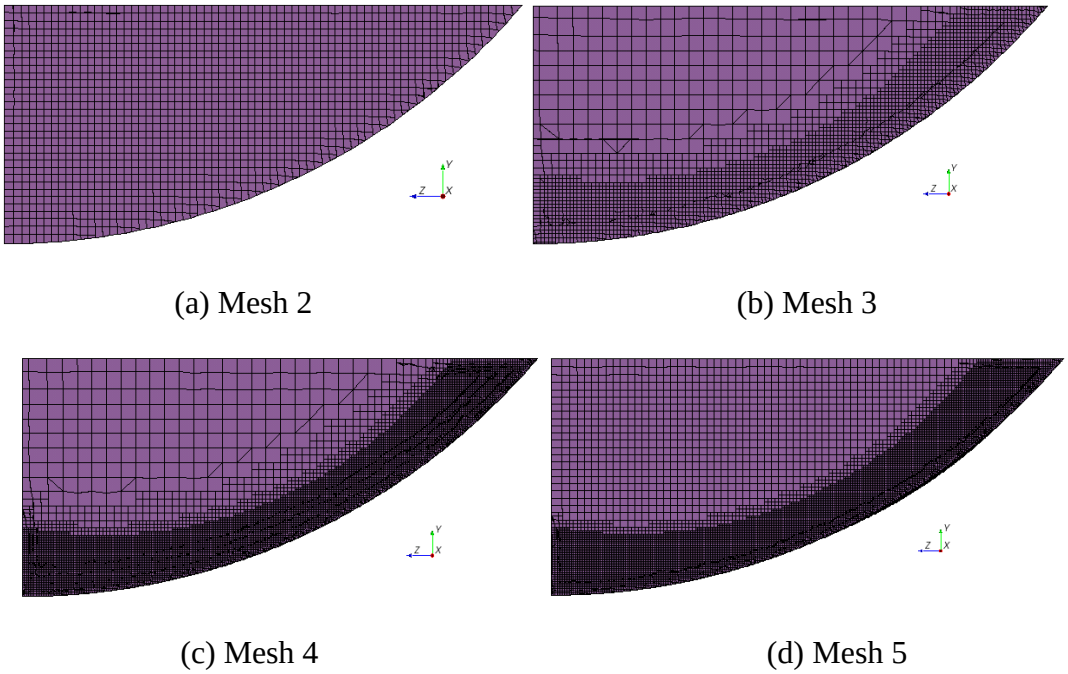

(a) Mesh 2 (b) Mesh 3

(c) Mesh 4 (d) Mesh 5

Figure 2.6: Mesh size distribution for different mesh types

The number of computational cells is increasing from Mesh 1 to 5 from about ten thousand cells in the coarse grid of mesh 1 to about 1 million cells in the very fine grid of mesh 5 as shown in Table 2.2. In addition several combinations of local refinement in the zone containing the corrugations were tested as shown in Figure 2.6. The figure does not show a coarser version of mesh 1 because it looks similar to mesh 2 with larger cells.

Obtaining a good quantitative measure of the quality of the computed result is not simple. The degree to which the computation can be converged is one measure of the quality of the results, and the mass residual is one quantitative measure of convergence. The closer to zero it is, the more highly converged the solution is. The mass residual for a base case test flow condition is listed in Table 2.2. All but the relatively coarse mesh 1, which did not converged below 10^{-3}, have mass residuals below 10^{-5}, which can be considered well converged. Depending on the geometry and the physics of the problem, however, very high levels of convergence can be obtained on very coarse meshes. The degree of convergence does not indicate the amount of discretion error. Without experimental data to compare against, the mass flow obtained by integrating over the cyclic boundary interface and a plane midway through the culvert section can be compared. Mass conservation requires the two values to be equal. When the flow is not parallel to the cells in the mesh, the difference in these values gives some indication of the discretization error. The corrugations cause the flow streamlines to curve and not remain parallel to the

mesh. The percent deviation of the mass flow across the boundary and mid planes is also listed in Table 2.2 for the meshes tested. For the coarse mesh 1, the deviation is nearly ½ percent. For the mesh with 60,000 cells it drops to 6 hundredths of a percent and to 2 hundredths of a percent for mesh 3 with 160,000 cells. At near a million cells the deviation drops to about 1 hundredth of a percent. Because the computation runs on one compute node and converges quickly in the range of 60,000 to 160,000 cells, and the mass flow deviations are also very small in this cell count range, meshes with cell counts in that range appear to be good candidates for use in a parametric study. Even the 1 million cell meshes can be used to obtain a solution for a parametric run case within a few hours on a single compute node running on eight cores. A further comparison of integrated axial flow velocities over strips on the cross section should be done before a final determination of the mesh to use for parametric study is made.

2.3.3. Sample Results for the Velocity Field

Sample simulation results for the velocity field are presented at two selected planes midway through the computational domain as shown in Figure 2.7. The first plane is created normal to the X-axis (along the flow direction) and the second plane normal to the negative Z-axis.

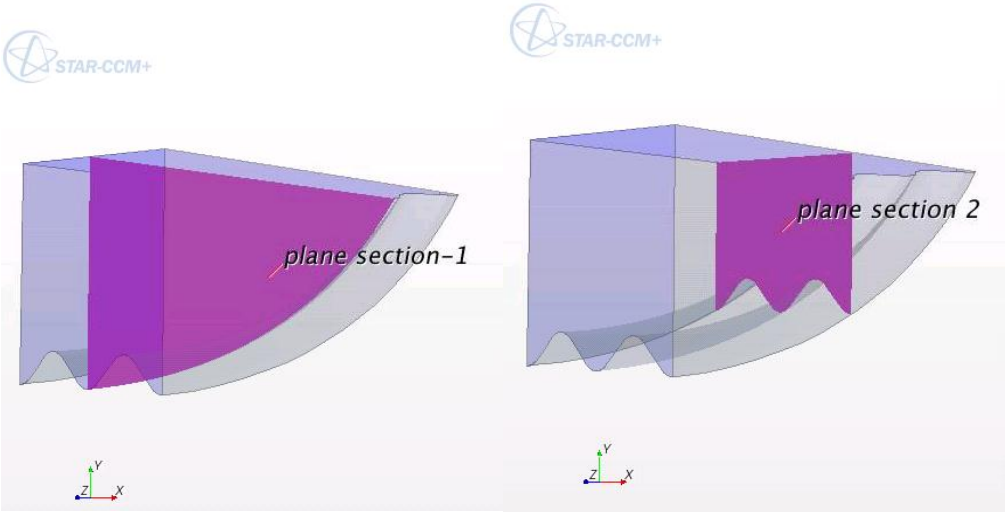

Figure 2.7: Planar sections for presentation of the simulation results

Figure 2.8 shows velocity magnitude contour plots for meshes 2 to 5. These are all qualitatively very close. The million cell mesh 5 in the lower right shows a bit more uniform velocity distribution away from the corrugations where fish would be swimming, indicating that a mesh with a bit more cell refinement in the core and a bit coarser mesh in the corrugation zone that would have 2 to 4 hundred thousand cells should be tested before a decision of the mesh to use for parametric runs is made.

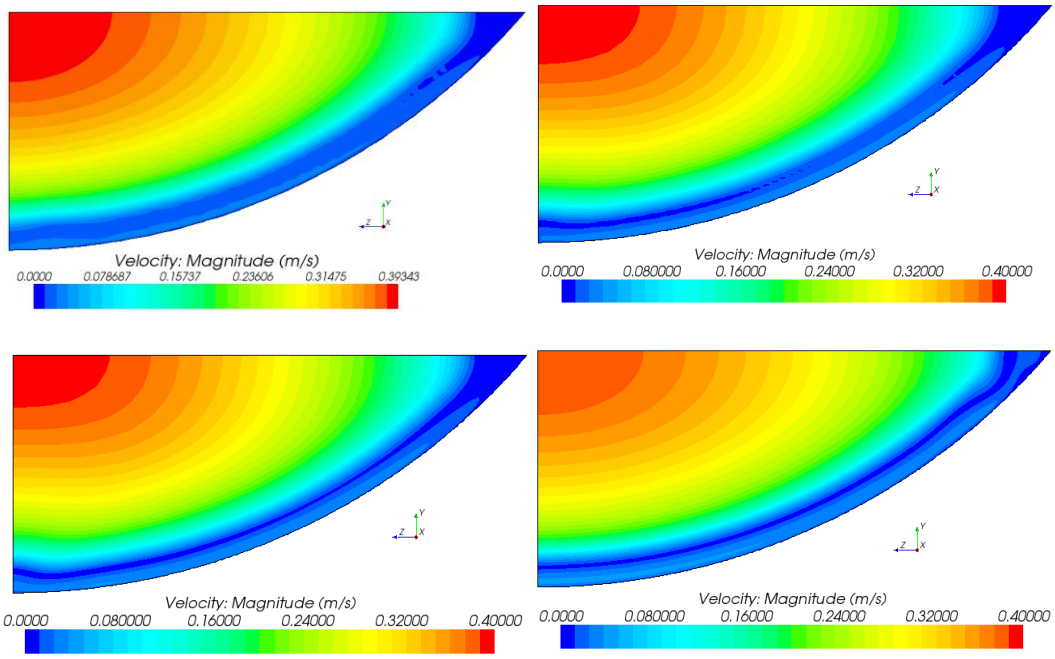

Figure 2.8: Cross section velocity distributions for meshes 2 to 5 respectively

Figure 2.9 shows the velocity magnitude on a plane cutting through corrugations. The nature of the fully developed flow velocity distribution is seen in the nearly uniform bands of the velocity contours that are only slightly disturbed by the corrugations in the region above the corrugations. The negative axial velocities in the lower portion of the troughs indicate the presence of recirculation zones, and matching patterns in whole trough and the half troughs on either side of the cyclic boundary indicate that the cyclic boundary condition is performing as desired.

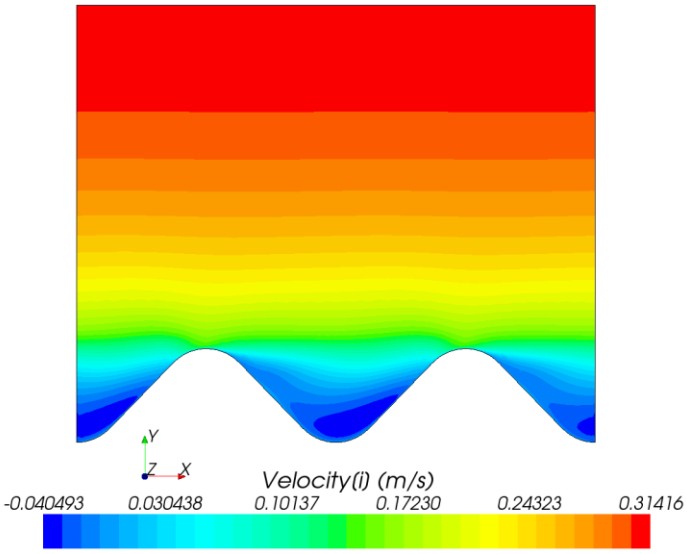

Figure 2.9: Velocity contour plot on a plane cutting through corrugations

2.3.4. Three Dimensional Model of Culvert Flume

The primary purpose of running CFD tests on a three dimensional model of the full TFHRC culvert test flume is to verify that the much smaller domain of a barrel section with cyclic boundary conditions can be used for parametric runs to determine zones for fish passage. A significant difference in the two models is that the small section using a cyclic boundary condition must be run as a single phase flow with a symmetric, free slip boundary condition at the water surface. This requires that the flow be deep enough for the corrugations to have negligible effect on the surface. CFD results from a full 3D model of the TFHRC culvert flume were compared to experimental data for several flow conditions in previous work and the CFD results were very close to the data [5]. The cases that were compared were all for a horizontal flume because that work was done before the TFHRC culvert flume could be tilted. The test described here uses a balanced combination of flap gate angle and flume tilt angle, but has not been compared against experimental data because the data is not yet available.

Based on the dimensional details provided by TFHRC, a CAD model of the full scale cross section of the culvert having annular corrugations was created as depicted in Figure 2.10. The model was been created in Pro-ENGINEER and imported to STAR-CCM+ in IGES (Initial Graphics Exchange Specification) file format for CFD analysis. This CAD model consists of three parts: the intake (inlet), the barrel section with corrugations and the diffuser (outlet).

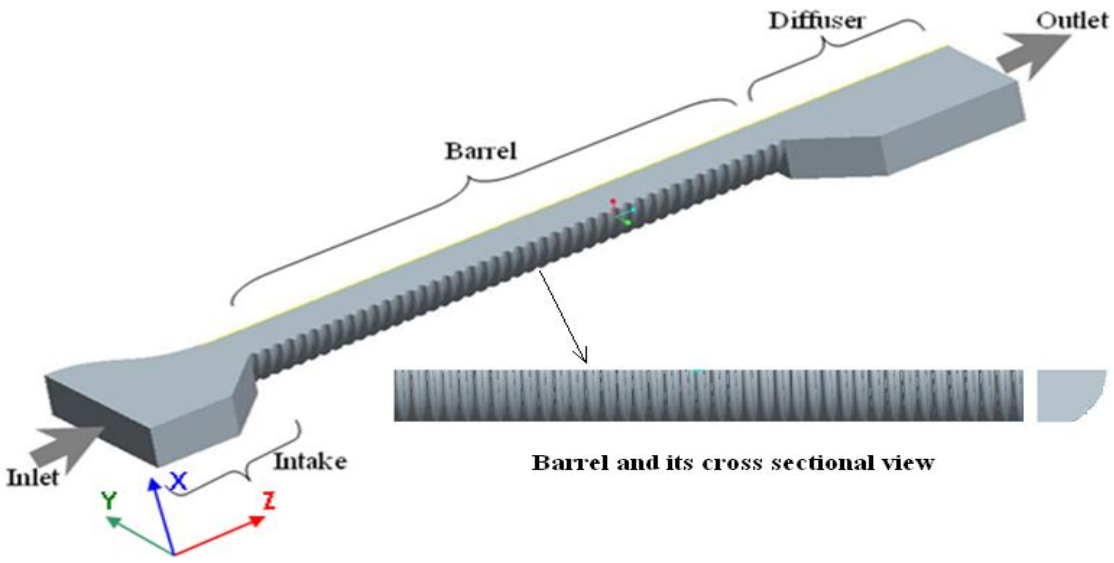

Figure 2.10: CAD model of the culvert flume

An enlarged view of the 3D flow domain in sections to show details of the mesh at the boundaries is shown in Figure 2.11 through Figure 2.13. The mesh shown was used for two phase simulation using the VOF model for flow with a free surface. The region of fine mesh a little above mid height was created to resolve the position of the free surface with reasonable accuracy.

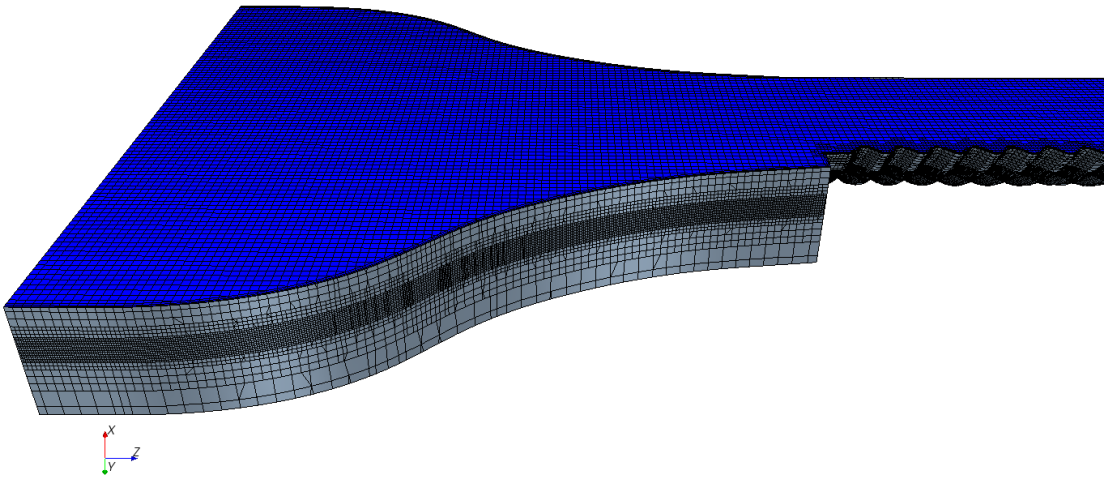

Figure 2.11: Meshed domain of the intake region

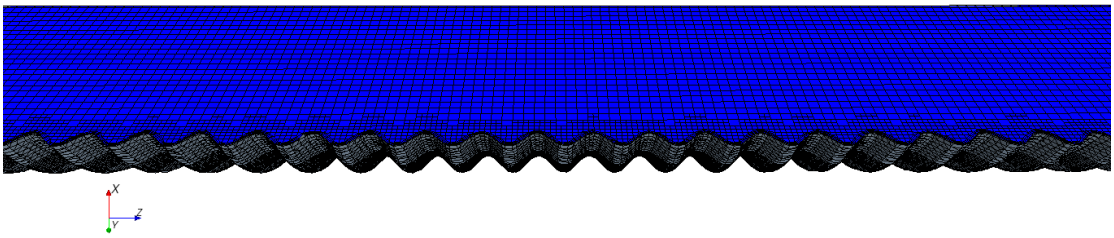

Figure 2.12: Meshed domain of the barrel region

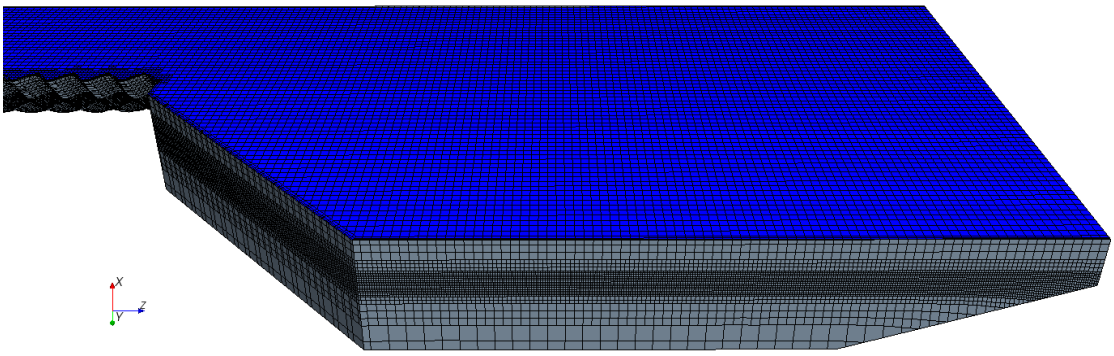

Figure 2.13: Meshed domain of the diffuser region

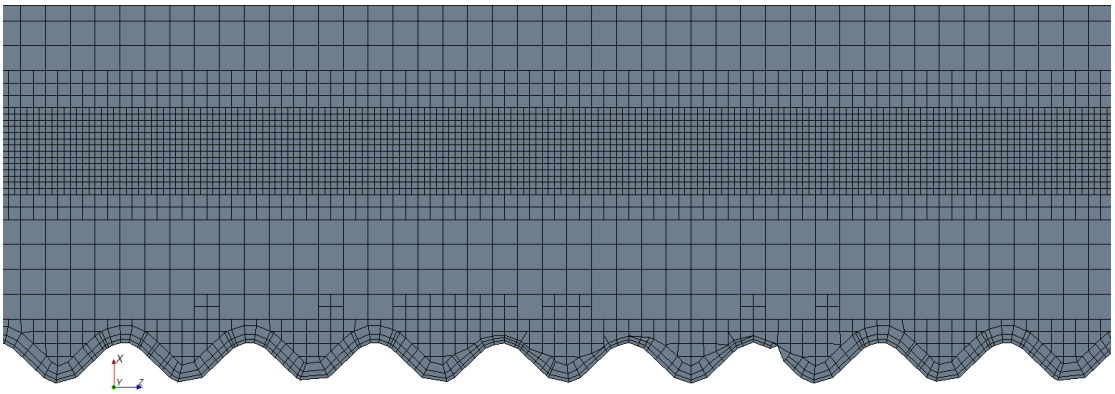

Figure 2.14: Enlarged view of the mesh on the left hand side of the flow direction

The corrugation in the model is 76.2 mm by 25.4 mm (3 by 1 inches) as shown in Figure 2.15.

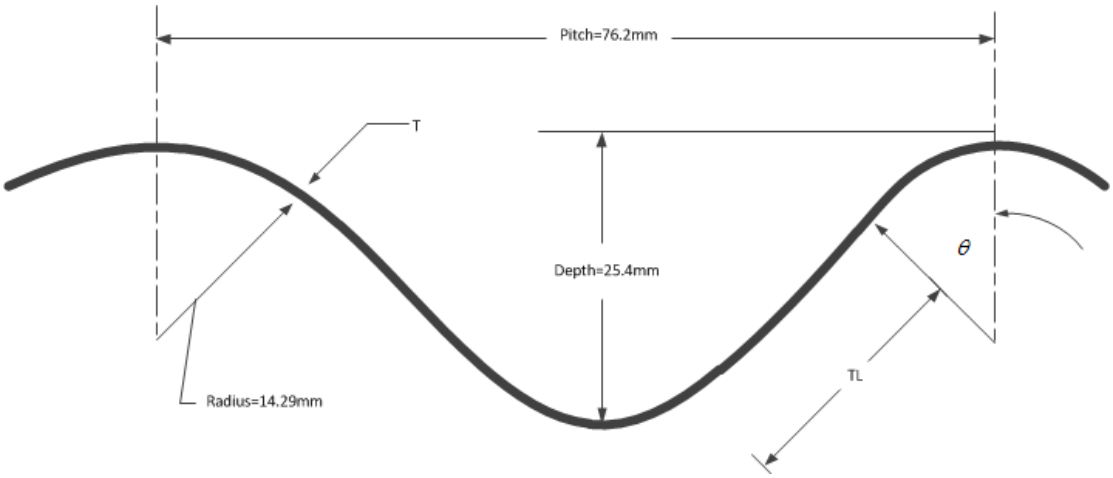

Figure 2.15: Corrugation profile of 76*25 mm (annular) (Handbook of Steel Drainage and Highway Construction)

Three typical cross sections were monitored in the tests, which were located at the inlet of the barrel (section 1), the middle of the barrel (section 2) and the end of the barrel (section 3), respectively.

2.3.5. Flow Conditions

(1) Flow depth is D/6 = 15.24 cm (6 in.), where D is the culvert diameter (36 in.)
(2) Bed elevation is 0
(3) Mean over a barrel cross section is 0.0344 m/s (0.71 ft/s)
(4) Tilting angle of the flap gate is 18 degree with respect to the horizontal
(5) The tilt angle of the flume is 0.125 degree.
(6) The geometry has half of the width culvert included with a smooth wall where the culvert centerline would be.

2.3.6. Results Using VOF Multiphase Model

The velocity distributions over the longitudinal section along the middle of the flume and the three cross sections for the multiphase model are shown in Figure 2.16. The highest velocity zone is near the vertical smooth wall boundary and spans the air-water interface.

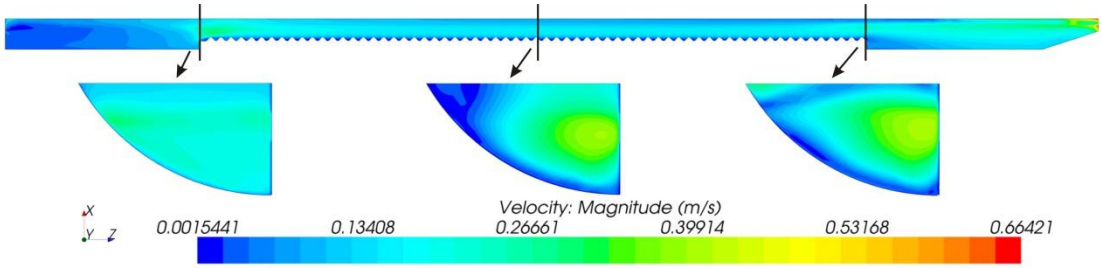

Figure 2.16: Velocity contour plots of the middle longitudinal section and cross-sections for the multiphase model

VOF distributions that show volume fraction of air (blue) and water (red) of the sections for the multiphase model are shown in Figure 2.17. A nearly uniform height water-air interface exists along the length of the barrel, and thus it appears likely that a single phase model can be used to simulate the flow of water under the interface with reasonable accuracy. Note that taking the 0.5 VOF iso-line as the air-water interface yields a water surface that coincides closely with the initial water level of 0.16D height.

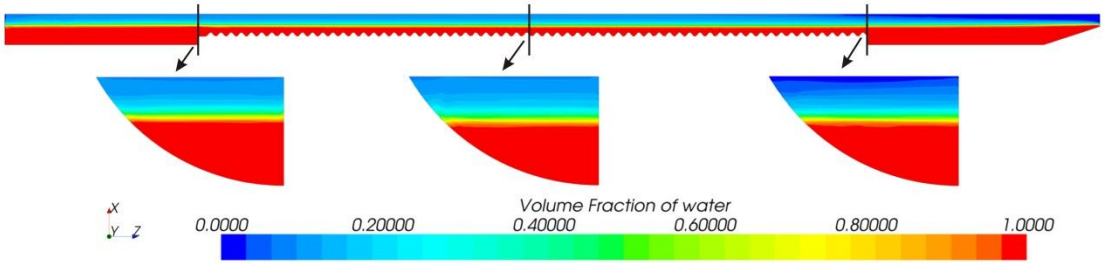

Figure 2.17: Volume fraction of water contour plot and three cross-sections distribution for the multiphase model

2.3.7. Comparison with the single phase model

A single phase model of the flow with a D/6 water depth was setup and run. The results from the steady state simulation for the velocity distribution are shown in Figure 2.18.

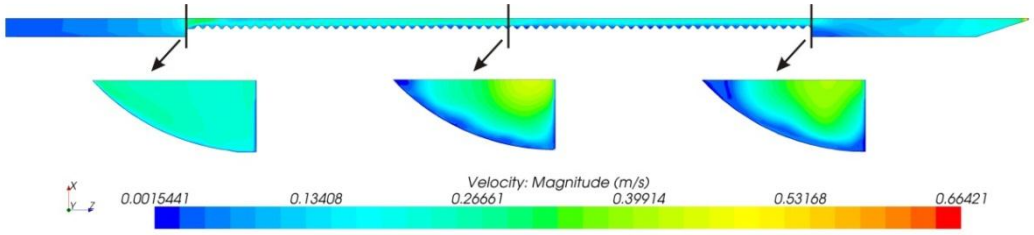

Figure 2.18: Velocity contour plots of the middle longitudinal section and cross-sections for the single phase model

A comparison of the velocity distributions between the single phase and the multiphase models in the three cross-sections is shown in Figure 2.19. The multiphase plots are cut at the D/6 water flow depth, which is the same height as the single phase flow domain. The 0.5 VOF curves are plotted on top of the velocity contours, and are slightly higher than the single phase water flow depth. The velocity of the single phase model is a little larger than that of the multiphase phase model because in the multiphase flow model the height of the free surface is computed and it is slightly higher than the planned water depth increasing slightly the cross section area carrying water. The small increase in water velocity when using the single phase model is conservative when doing analysis to determine if the flow permits fish passage. Single phase flow CFD analysis of culvert flows under conditions where the free surface is nearly flat appears adequate for fish passage assessment, greatly reduces computational resources and computation time, and therefore would be the preferred and recommended method when the flow condition requirements are met.

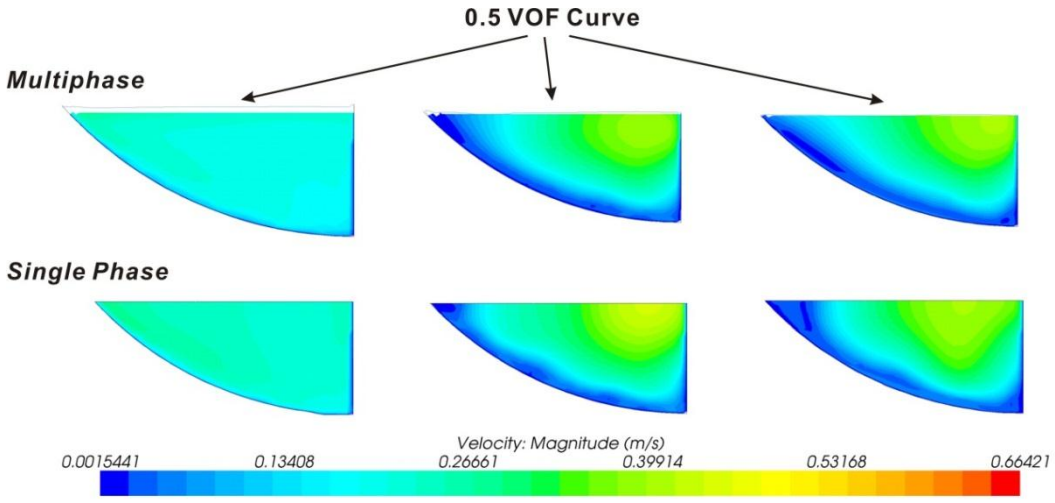

Figure 2.19: Comparison of velocity distribution for the multiphase model and single phase model

2.3.8. References

1. Matt Blank, Joel Cahoon, Tom McMahon, “Advanced studies of fish passage through culverts: 1-D and 3-D hydraulic modeling of velocity, fish expenditure and a new barrier assesment method,” Department of Civil Engineering and Ecology, Montana State University, October, 2008 .

2. Marian Muste, Hao-Che Ho, Daniel Mehl,“Insights into the origin & characteristic of the sedimentation process at multi barrel culverts in Iowa”, Final Report, IHRB, TR-596, June, 2010.

3. Liaqat A. Khan, Elizabeth W.Roy, and Mizan Rashid, “CFD modelling of Forebay hydrodyamics created by a floating juvenile fish collection facility at the upper bank river dam”, Washington, 2008.

4. Angela Gardner, “Fish Passage Through Road Culverts” MS Thesis, North Carolina State University, 2006.

5. Vishnu Vardhan Reddy Pati, “CFD modeling and analysis of flow through culverts”, MS Thesis, Northern Illinois University, 2010.

6. Kornel Kerenyi, “Final Draft, Fish Passage in Large Culverts with Low Flow Proposed Tests” unpublished TFHRC experimental and CFD analysis of culvert flow for fish passage work plan, 2011.

2.4. Training on CFD Analysis for Hydraulics and Wind Engineering Applications

Training on and technology transfer of high performance computational analysis techniques is an important part of Argonne’s work to support and advance engineering and research programs at TFHRC. The first training course in the application of CD-adapco’s STAR-CCM+ CFD software was conducted on March 30-31, 2011. The course included five tutorials relevant for hydraulics and wind engineering applications. Four of the tutorials were developed specifically for the course and two covered the basic techniques being developed for culvert and scour analysis that are covered in the technical sections of this report.

3. Computational Multiphysics Mechanics

3.1. Multiphysics Simulation of Salt Spray Transport

The Turner Fairbank Highway Research Center (TFHRC) currently is interested in studying the transport of salt spray generated by vehicle tires from the pavement up to the exposed steel support beams of steel bridges as the tires roll over wet pavement. The research is aimed to update the Technical Advisory, which is already over 20 years old, with results based on current state-of–the-art computational analysis and experimental data acquired at critical locations.

In the last quarter TRACC has received plans of four excessively rusting bridges in West Virginia and New York Divisions:

- West Virginia:
  - Raleigh - Tamarack Overpass (Bridge No. 4172)
- New York Division:
  - Kendrick Road (BIN 4443840)
  - West Henrietta (BIN 1070290)
  - East Henrietta (BIN 1070900)

Based on blueprints of the Bridge No. 4172 in West Virginia, an initial multiphysics model was developed to represent a large semi-trailer truck traveling under the bridge. The LS-DYNA/MPP model uses the Multi-Material Arbitrary Lagrangian-Eulerian formulation as described in detail in the previous report. The model captures all the geometric characteristics of the bridge and the truck. Both are modeled as rigid bodies since their deformation is irrelevant for this problem. Initial runs were performed for the semi-trailer truck traveling at 60 MPH speed through the air MM-ALE domain (see Figure 3.1:). In the simulations tracer particles were defined in the air at different levels under the bridge beams. Their movement was then traced in the post-processing. Figure 3.2: shows some of the particles at different time instances of the calculation. It can be clearly seen that some of the air particles are getting raised to the level of the bridge deck. Once the salt spray is lifted up from the road surface it can be easily transported to the steel beams.

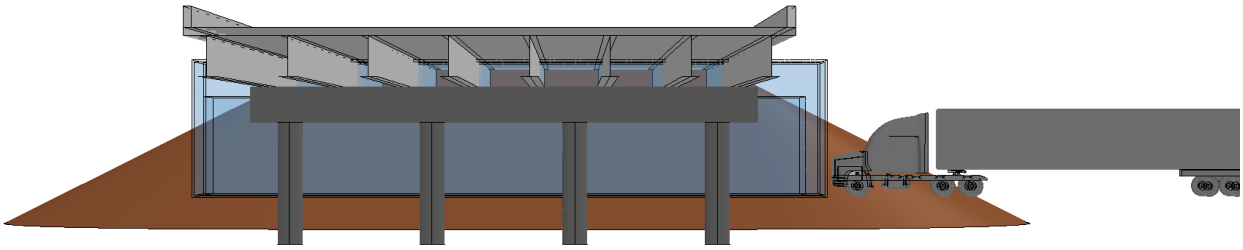

Figure 3.1: Setup for analysis of the air movement under the bridge

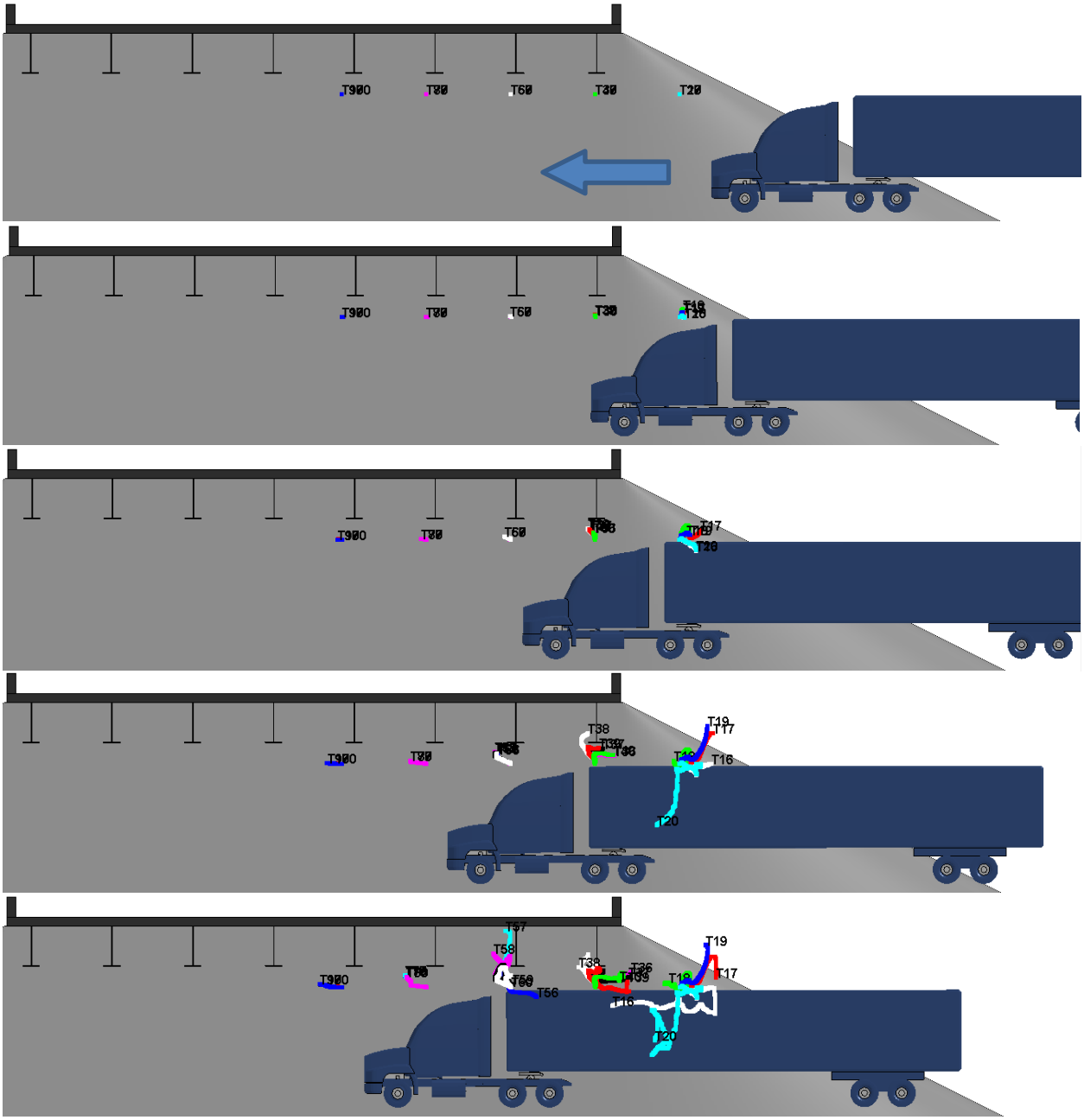

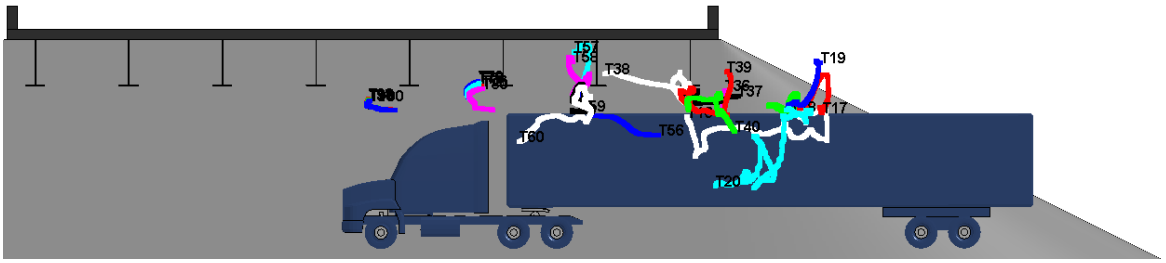

Figure 3.2: Snapshots from the LS-DYNA simulation of the truck passage under the bridge

The analysis is currently at its initial stage. Since the newest capabilities of the software are used, there is no well-defined procedure on how to analyze such problems. Appropriate modeling techniques for this multiphysics problem being developed. In the next quarter TRACC staff will focus on:

- improving the current simulation;
- introducing multiple vehicles into the simulation;
- including spray injectors in the road surface to simulate the salt spray;
- perform parametric study on the bridge geometry.

3.2. Wind Engineering

Understanding the interaction of wind on fixed structures (e.g., bridges) and/or moving vehicles (e.g., automobiles, trucks, buses) and the interaction between vehicles and bridges can lead to safety enhancements. For example, understanding wind-vehicle interaction can lead to speed guidelines for vehicles traveling over bridges during high wind conditions. Evaluating the structural response of bridges to extreme wind loading can lead to safer bridge designs. This section will periodically report on work being done by TRACC's Computational Structural Mechanics Section on several Wind Engineering research areas.

3.2.1. Vehicle Stability under High Wind Loadings

The following work was started as a joint effort between Northern Illinois University (Prof. Abhijit Gupta and his student Rohan Patil) and TRACC staff members Ron Kulak and Cezary Bojanowski. The task was to conduct a literature review to become familiar with the issues and then perform research on the identified open issues. This section mostly presents finding from the literature review.

Table 3.1 list the factors that contribute to vehicle dynamics [1].

To understand vehicle dynamics, it is important to identify the forces acting on the vehicle. Chen and Chen [2] described the primary forces acting on a vehicle. The lateral tire force perpendicular to the direction of velocity at the wheel ground contact patches is proportional to tire slip angle.

$$F_{y,f} = \mu * c_f * \alpha_f = \mu * c_f * (-\beta + \delta - a_f * \frac{\dot{\psi}}{V}) \quad (3.1)$$

$$F_{y,r} = \mu * c_r * \alpha_r = \mu * c_r * (-\beta + \delta - a_r * \frac{\dot{\psi}}{V}) \quad (3.2)$$

Where c_i is the tire slip constant and α_i is the tire side slip angle associated with the front and rear axles, μ is the road adhesion coefficient and β,δ,ψ are side slip angle, steer angle and yaw rate respectively. V is the velocity of the vehicle and a_f and a_r are longitudinal distances from the center of the sprung mass to the front axle.

Table 3.1: Factors affecting Vehicle Dynamics [2]

Aerodynamic specific	**Driving techniques**
Automobile drag coefficient	Cadence braking
Automotive aerodynamics	Threshold braking
Center of pressure	Double declutching
Down force	Drifting (motorsport)
Ground effect in cars	Handbrake turn
Mass specific	Heel-and-Toe
Center of mass	Left-foot braking
Moment of inertia	Opposite lock
Sprung mass	Scandinavian flick
Unsprung mass	**Motion specific**
Weight distribution	Body flex
Tire specific	Bump Steer
Camber thrust	Directional stability
Circle of forces	Critical speed
Contact patch	Load transfer
Cornering force	Noise, vibration, and harshness
Ground pressure	Oversteer
Pacejka's Magic Formula	Ride quality
Pneumatic trail	Speed wobble
Relaxation length	Understeer
Rolling resistance	Weight transfer
Self aligning torque	
Slip angle	
Slip (vehicle dynamics)	
Steering ratio	
Tire load sensitivity	

Cross wind forces: The crosswind induced quasi static forces and moments acting on the vehicle on x, y and z axis are defined in the following manner.

Drag Force: $$F_x = 0.5 * \rho * C_{Fx} * A * V_{re}^2 \quad (3.3)$$

Lift Force: $$F_y = 0.5 * \rho * C_{Fy} * A * V_{re}^2 \quad (3.4)$$

Side Force: $$F_z = 0.5 * \rho * C_{Fz} * A * V_{re}^2 \ \ldots \quad (3.5)$$

Rolling Moment: $$M_x = 0.5 * \rho * C_{Mx} * A * V_{re}^2 * h_{re} \quad (3.6)$$

Yawing Moment: $$M_y = 0.5 * \rho * C_{My} * A * V_{re}^2 * h_{re}. \quad (3.7)$$

Pitching Moment: $$M_z = 0.5 * \rho * C_{My} * A * V_{re}^2 * h_{re} \quad (3.8)$$

here ρ is the density of air, A is the reference area, V is the vehicle straight speed taken as the relative velocity of the air, h_{re} is the reference arm, C_{FX}, C_{FY}, C_{FZ} are wind force coefficients and C_{Mx}, C_{My}, C_{Mz} are related to the shape of a vehicle.

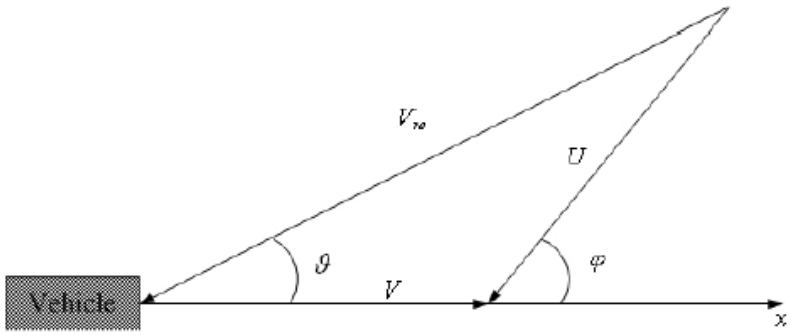

Figure 3.3: Addition of velocity vectors [2]

Figure 3.3 shows the vector relationship of the velocities. Here, V represents the relative velocity of air caused by the vehicle speed, U is the wind velocity, ψ is wind direction, V_{re} is the relative wind velocity and υ is the angle of incidence.

A simplified roll-plane model has been developed by Winkle and Ervin [3] and a terse overview of their work is presented here Figure 3.4 represents a simplified model of a heavy vehicle in a steady turn in which the vehicle, its tires and suspensions have been lumped into a single rolling plane. The equilibrium equation for rolling moment about a point on the ground at the center of the track is given by:

$$W \cdot h \cdot a_y = (F2 - F1) \cdot \left(\frac{T}{2}\right) - W \cdot \Delta y \quad (3.9)$$

where, a_y is lateral acceleration, F_i are the vertical tire loads, h is the height of cg, T is the track width, W is the weight of the vehicle, Δy is the lateral motion of the cg relative to the track, ϕ is the roll angle of the vehicle. The quantities in Equation 3.9 are defined in Figure 3.4.

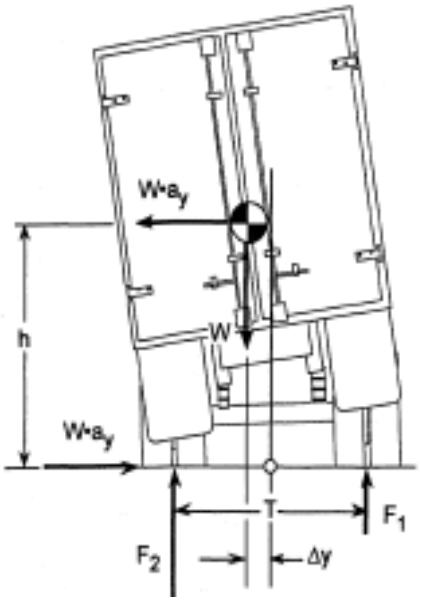

Figure 3.4: Simple roll plane model [3]

The basic dynamic model (Figure 3.5) gives the equation of forces acting on the vehicle. In this model, pitching and bouncing motion is not considered as it affects the rolling and handling behavior of the vehicle insignificantly. The sprung mass rotates about the roll center depending upon the suspension properties. The unsprung masses also can rotate, combined with the effect of the vertical compliance of the tires. Applying the change in momentum and summation of external forces, the equations of vehicles motions are obtained. The suspension parameters like damping coefficients are assumed to be constant.

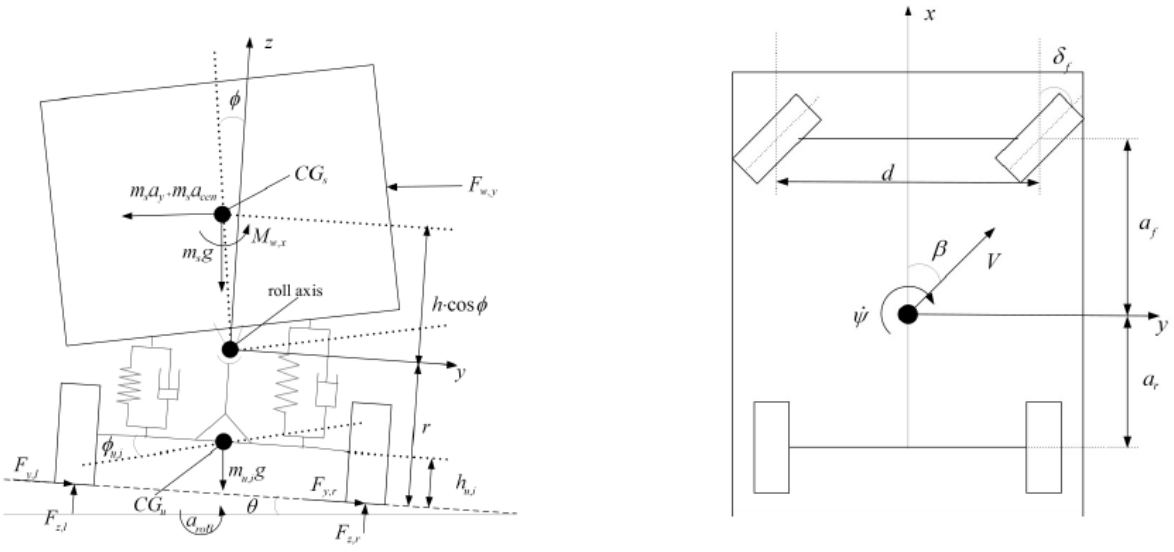

Figure 3.5: Single body vehicle model[2]

Considering the wind load, road camber and bridge acceleration, the five equilibrium equations of vehicle motions of sprung mass and suspensions are given as follows:

$$m_s * h * \ddot{\phi} = m * V * \left(\dot{\beta} + \dot{\psi}\right) - F_{y,f} - F_{y,r} + F_{w,y} - m * g * \theta + m * a_y \tag{3.10}$$

$$-I_{xz} * \ddot{\phi} + I_{zz} * \ddot{\psi} = F_{y,f} * a_f + F_{y,r} * a_r + M_z \tag{3.11}$$

$$\begin{aligned} I_{xx}\ddot{\phi} - I_{xz}\ddot{\psi} = {} & m_s * g * h * \phi + m_s * V * h\left(\dot{\beta} - \dot{\psi}\right) + M_x - m_s * g * h * \theta + m_s \\ & * g * a_y + F_{w,y} * h_w - k_r\left(\phi - \phi_{t,f}\right) - l_f\left(\dot{\phi} - \dot{\phi}_{t,f}\right) + u_f \\ & - k_r\left(\phi - \phi_{t,r}\right) - l_r\left(\dot{\phi} - \dot{\phi_{t,r}}\right) + u_r \end{aligned} \tag{3.12}$$

$$\begin{aligned} rF_{y,f} = {} & -m_{u,f} * V\left(h_{u,f} - r\right) * \left(\dot{\beta} + \dot{\psi}\right) + m_{u,f} * g * \left(h_{u,f} - r\right) * \phi_{t,f} + m_{u,f} \\ & * g\left(h_{u,f} - r\right) * \theta - a_{roll} * I_{xx} * m_f - m_{u,f} * a_y\left(h_{u,f} - r\right) + k_{t,f} \\ & * \phi_{t,f} - k_f\left(\phi - \phi_{t,f}\right) - l_f\left(\dot{\phi} - \dot{\phi_{t,f}}\right) + u_f \end{aligned} \tag{3.13}$$

$$\begin{aligned} rF_{y,r} = {} & -m_{u,r} * V\left(h_{u,r} - r\right) * \left(\dot{\beta} + \dot{\psi}\right) + m_{u,r} * g * \left(h_{u,r} - r\right) * \phi_{t,r} + m_{u,r} \\ & * g\left(h_{u,r} - r\right) * \theta - a_{roll} * I_{xx} * m_r - m_{u,r} * a_y\left(h_{u,r} - r\right) + k_{t,r} \\ & * \phi_{t,r} - k_r\left(\phi - \phi_{t,r}\right) - l_f\left(\dot{\phi} - \dot{\phi_{t,r}}\right) + u_r \end{aligned} \tag{3.14}$$

where $F_{w,y}$, M_x, M_z are lateral wind force, wind induced roll moment and wind-induced yaw moment, θ is road camber, a_y is acceleration of the bridge; *a roll* is the rolling acceleration of the bridge, *k is* tire roll stiffness, *L is* wheelbase, l suspension roll damping rate, M_x wind-induced roll moment, M_z wind-induced yaw moment, *m* total mass, m_s sprung mass, m_u unsprung mass, *r* height of roll axis, measured upwards from ground, *U* forward speed, *u* active roll torque, α tire slip angle, β sideslip angle, δ steer angle, ϕ absolute roll angle of sprung mass, ϕ_τ absolute roll angle of unsprung mass, ϕ_τ^* roll angle of unsprung mass when one wheel lift up and Ψ heading angle.

The criterion for wheel lift was presented by Chen and Chen [2]. The weight transfer equations of the vehicle body can be calculated by summation of moments about a point located at the mid-track along the ground to obtain:

$$\begin{aligned} W_{trans} = {} & \left(m * V\left(\dot{\beta} + \dot{\psi}\right) + m * a_y + m * g(\phi - \theta)\right) * h_{cm} \\ & + \frac{F_{w,y}(h_w + r) + M_x + a_{roll} * I_{xx})}{d} \end{aligned} \tag{3.15}$$

For the purpose of the students becoming familiar with LS-DYNA, which will be used for studying three-dimensional vehicle dynamics subjected to wind loading, some very simple models were exercised. In order to gain clear understanding of the project, the initial phase was started with a simple “block” model of a truck (Figure 3.6). The model consists of a “block” representing the truck body mounted on four spring dampers representing the suspension system. The model is constrained to allow only vertical motion. The model is subjected to an initial downward velocity. The parameters used in the simulation are given in Table 3.2.

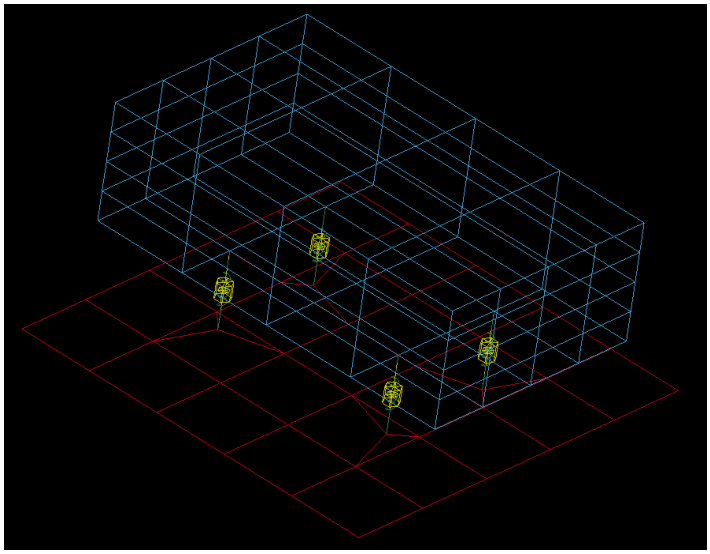

Figure 3.6: Block Model of a truck

Table 3.2: Simulation parameters

Quantity	Value
Stiffness (K)	1,000 N/mm
Mass (m)	235.5 10^3 Kg
Damping	10 N-s/mm
Initial Velocity	-5,000 mm/s

This simplified model has a closed form analytical solution and the result for the vertical displacement of the truck subjected to an initial vertical velocity is shown in Figure 3.7 for the case with zero damping. The results from the LS-DYNA simulation are shown in Figure 3.8 and are seen to be identical in magnitude and frequency.

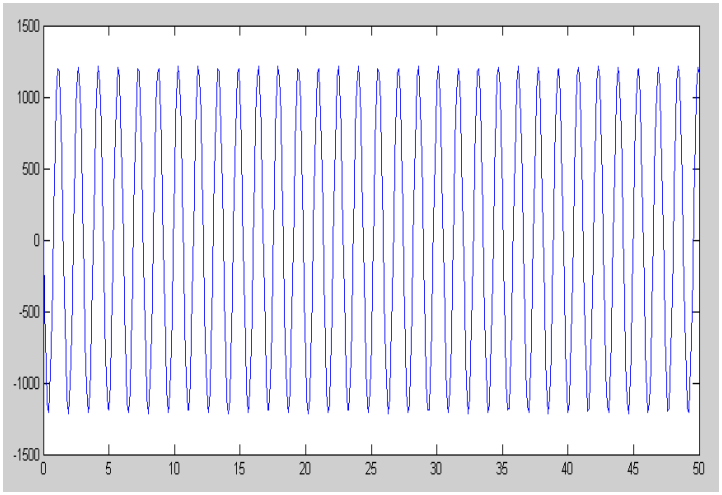

Figure 3.7: Analytical solution for vertical time history

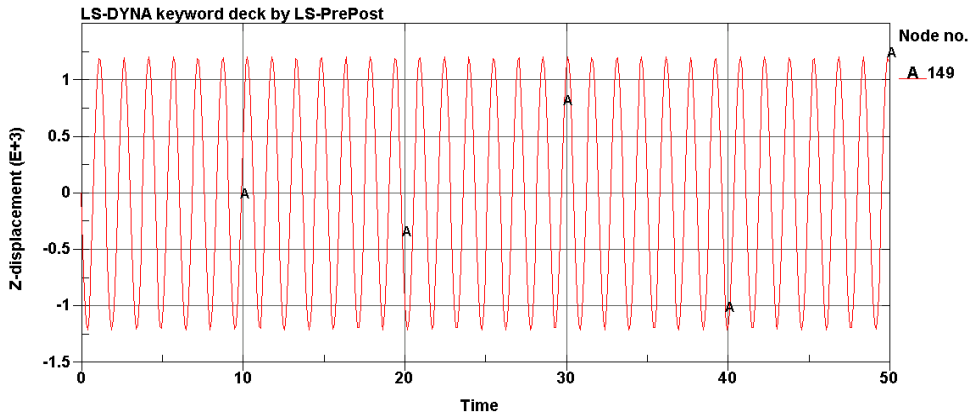

Figure 3.8: LS-DYNA solution for vertical time history

When damping is included, the comparisons between analytical and numerical solution are also seen to be very good (Figure 3.9 and Figure 3.10)

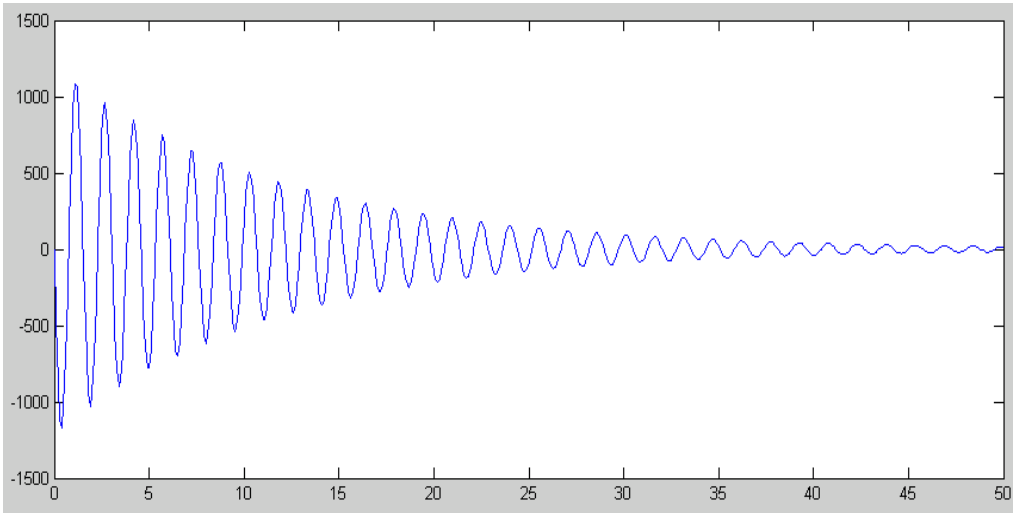

Figure 3.9: Analytical solution for vertical displacement with damping

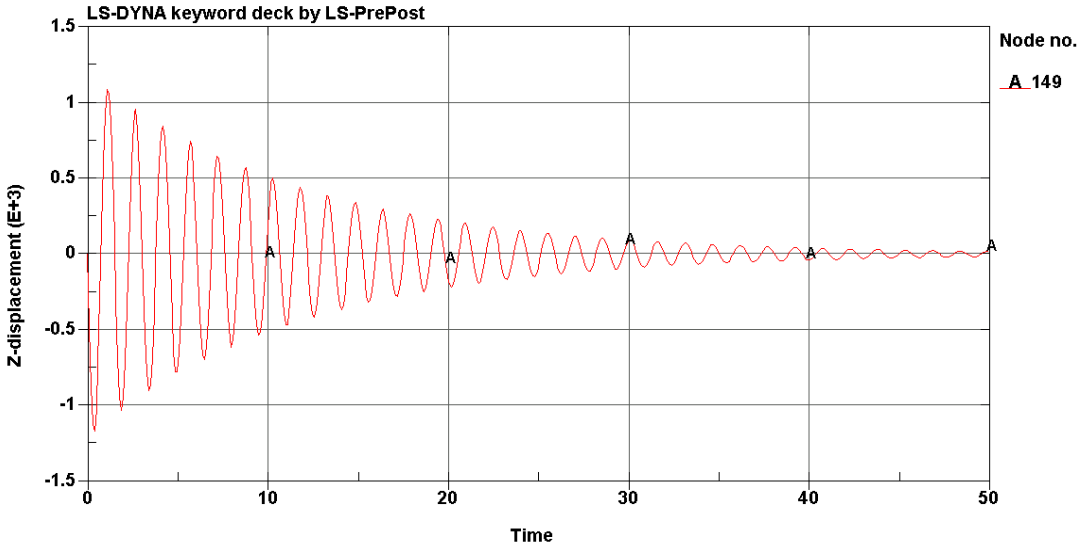

Figure 3.10: LS-DYNA solution for vertical displacement with damping

3.2.2. Electromagnetic Shock Absorber for Vehicle Stability under High Wind Conditions

Introduction

Vehicle suspension systems are an important aspect to the overall performance of a vehicle. Suspension systems provide comfort, handling/performance and safety. Comfort is achieved by providing isolation to the sprung mass (Vehicle body) from any outside disturbances which may include: the road profile, potholes, speed bumps, strong wind effects, sudden turn and/or hard braking/acceleration. Good handling provides the car with a strong contact between the road and the tires. Safety is achieved by a harmonious design providing both comfort and suitable performance. Comfort and handling are in direct conflict with each other. A high performance suspension system will allow the user to take tight turns but the user will also feel all of the disturbances due to the road profile. On the other hand a luxury vehicle will provide a high comfort level but the performance of the vehicle is hindered, i.e. tight turns and maneuvering are hard to achieve.

Suspension systems are generally separated into three broad categories, which are: passive, semi-active and active systems. Passive systems have fixed suspension properties and are used most often. They are reliable, cheap and easy. Semi-active systems provide a variable damping coefficient to provide control of the system. These systems are limited because the force will always be proportional to the relative velocity as seen by the suspension; this also limits the direction of the force. Active systems can provide a force based upon any number of states. These systems provide the best performance and comfort. However, they tend to be more expensive, heavy, unreliable, costly and consume more power than semi-active and passive systems.

Suspension control is not a new concept; research began around the mid 1970's [4]. And the first vehicle to be productively manufactured with a semi-active electronically controlled suspension system was the Mitsubishi Gallant back in 1987. The applications for suspension control include improved performance

in terms of handling, comfort and safety. This is not an easy task since comfort and performance are in direct conflict with each other. The major distinctions between the current research papers include: modeling of the suspension, the type of controllable input used, and the type of control strategy used to develop the controller. Research papers vary from using a SDOF, ¼ car, ½ car and full car models; as well as including the passive elements of the suspension or replacing them with a new element. The type of controllable input used can be a damping force or a general force and the actual element providing the force can be pneumatic, motor/actuator, electromagnetic shock absorber (EMSA) and others. Another major distinction is the control strategy used to develop the actual controller. The control strategy used for this project will be Linear Quadratic Regulator/Gaussian (LQR or LQG). In the remainder of the report the control strategy will be referred to as LQR. LQR has the ability to improve both comfort and handling but it requires full state measurement or at the very least a very good estimate [5]. If full state measurement is not possible, then an estimator will be used, which behaves just like a typical controller.

The major distinctions between this project and the other projects are that this project focuses on a vehicle traveling under high wind and/or other outside adverse effects rather than just the road profile. Majority of the current research projects do not evaluate the controller design via an FEM simulation. Also, the properties for the truck model used in this project will be obtained directly from a Ford F800 single-unit truck model, developed by the Federal Highway Administration (FHWA) through the National Crash Analysis Center (NCAC). The evaluation of the controller design will be done using the F800 model with LS-DYNA. This effectively ensures more practical results, given that the F800 model is extremely detailed and precise.

Conventional Quarter Car Model

Shown in Figure 3.11 is the conventional quarter car model [6]. This model provides information on bounce mode only (vertical deflection); other models such as ½ car and full-car provide information on pitch and roll. However, majority of the current research in this topic utilize the quarter car model due to its simplicity and its ability to provide useful insight into the dynamics of the vehicle. The sprung mass denoted by M_s represents the mass of the vehicle body; in this case it will equal ¼ the total vehicle body mass. X_s is the position of the sprung mass. The unsprung mass denoted by M_u represents the mass of the wheel, hub and the brake assembly. X_u is the position of the wheel. The suspension is modeled by using a spring damper combination (k_s and c_s). Semi-active and active systems will have either another element placed in the suspension which can produce a variable force or by replacing the whole system with an actuator. U denotes the road profile, which is considered to be an input in this model, since no control is involved. The tire has stiffness but the damping is very minimal and is taken to be zero, the stiffness of the tire is denoted k_t.

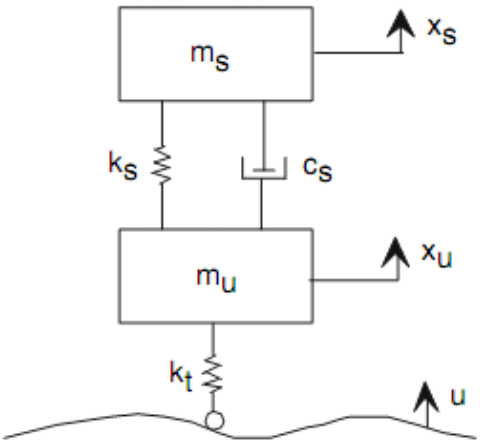

- **m_s = Sprung mass, vehicle body**
- **x_s = Position of vehicle body**
- **k_s = Suspension spring constant**
- **c_s = Suspension damping constant**
- **m_u = Unsprung mass, wheel/hub**
- **x_u = Position of wheel**
- **k_t = Tire spring constant**
- **u = Road profile**

Figure 3.11: Conventional Quarter Car Model

EMSA Quarter Car Control Model

Figure 3.12 shows the EMSA quarter car control model. It was obtained by modifying Figure 3.11. Here u is no longer the road profile, which is now denoted by x_r. The damping force input is now denoted by u. The model maintains the passive elements of the suspension system but incorporates a controllable semi-active EMSA. The EMSA will provide the damping force u(t). This model was selected for two reasons, one because it will allow for an easy comparison between passive, semi-active and active systems. By setting u(t) to be zero, the system will be passive, and by setting u(t) to be a function based upon the controller without the consideration of the EMSA, the system will be active. By setting u(t) to be based upon the controller and the EMSA model, the system will be semi-active. The other reason the model was selected is a practical reason; if the EMSA were to fail the truck will still be left with the passive suspension and during normal operation the power consumption of the EMSA will be minimal, since the passive elements take care of most of the energy absorption/transfer.

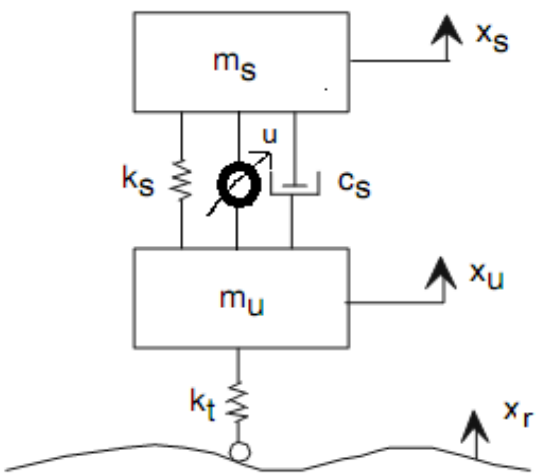

- **m_s = Sprung mass, vehicle body**
- **x_s = Position of vehicle body**
- **k_s = Suspension spring constant**
- **c_s = Suspension damping constant**
- **m_u = Unsprung mass, wheel/hub**
- **x_u = Position of wheel**
- **k_t = Tire spring constant**
- **x_r = Road profile**
- **u = External input damping force**
- **Notice: u is now the force input, no longer the road profile which is now denoted x_r**

Figure 3.12: Quarter Control Car Model

The equations of motion for the sprung and unsprung masses of the quarter-car control model are given by:

At M_s

$$M_s \cdot \frac{d^2}{dt^2} X_s + c_s \cdot \left(\frac{d}{dt} X_s - \frac{d}{dt} X_u \right) + k_s \cdot \left(X_s - X_u \right) = -u(t) \tag{3.16}$$

At M_u

$$M_u \cdot \frac{d^2}{dt^2} X_u + c_s \cdot \left(\frac{d}{dt} X_u - \frac{d}{dt} X_s \right) + k_s \cdot \left(X_u - X_s \right) + k_t \cdot \left(X_u - X_r \right) = u(t) \tag{3.17}$$

In order to develop a controller for the system, states of interest have to be determined. After this the Equations of motion along with the states of interest are then put into state-space form. The state variables are chosen as:

$$X_1 = X_s(t) - X_u(t) \qquad X_2 = X_u(t) - X_r(t) \qquad X_3 = \frac{d}{dt} X_s(t)$$

$$X_4 = \frac{d}{dt} X_u(t) \qquad \text{With disturbance: } w(t) = \frac{d}{dt} X_r(t) \tag{3.18}$$

These states were chosen for the following reasons: The positions of X_s, X_u and X_r are obviously important but the difference between these values yields more information upon the system; the other important variables to consider are the accelerations of the sprung and unsprung masses [7]. In the state-space formulation, X is a vector representing the states, which are variables in $\dot{X}$. So, X_3 and X_4

automatically incorporate the acceleration of both masses. Note that the disturbance term is needed due to X_2 involving the variable X_r. The state-space takes the general form of:

$$\frac{d}{dt}X(t) = A\cdot X(t) + B\cdot u(t) + B_w\cdot w(t) \tag{3.19}$$

Where A is a nXn constant coefficient matrix, with n being equal to the number of states. B and B_w are nX1 constant coefficient vectors. X(t) are the states and is a nX1 vector, u(t) is the control force which is a scalar input and w(t) is the time derivative of the road profile which is a scalar value. Thus the state-space formulation is:

$$\begin{pmatrix} \frac{d}{dt}X_1 \\ \frac{d}{dt}X_2 \\ \frac{d}{dt}X_3 \\ \frac{d}{dt}X_4 \end{pmatrix} = \begin{pmatrix} 0 & 0 & 1 & -1 \\ 0 & 0 & 0 & 1 \\ \frac{-k_s}{M_s} & 0 & \frac{-c_s}{M_s} & \frac{c_s}{M_s} \\ \frac{k_s}{M_u} & \frac{-k_t}{M_u} & \frac{c_s}{M_u} & \frac{-c_s}{M_u} \end{pmatrix} \cdot \begin{pmatrix} X_1 \\ X_2 \\ X_3 \\ X_4 \end{pmatrix} + \begin{pmatrix} 0 \\ 0 \\ \frac{-1}{M_s} \\ \frac{1}{M_u} \end{pmatrix} \cdot u(t) + \begin{pmatrix} 0 \\ -1 \\ 0 \\ 0 \end{pmatrix} \cdot w(t) \tag{3.20}$$

Formulation of LQR controller

First of all the system has to be controllable before any other work is performed. The controllability matrix will provide this information. The controllability matrix needs full rank in order for the system to be controllable. A matrix with full rank is equivalent to a matrix with a non-zero value for its determinate. The controllability matrix is a nXn matrix with the first column equal to the vector B, the next column is equal to the product of matrix A and vector B and the next column is the product of A^2 and B. This repeats for the remaining columns until the last column is found by the product of $A^{(n-1)}$ and B. The controllability matrix, C, is shown below:

$$C = \begin{pmatrix} B & A\cdot B & A^2\cdot B & A^3\cdot B \\ B & A\cdot B & A^2\cdot B & A^3\cdot B \\ B & A\cdot B & A^2\cdot B & A^3\cdot B \\ B & A\cdot B & A^2\cdot B & A^3\cdot B \end{pmatrix} \tag{3.21}$$

$$|C| \neq 0$$

$$|C| = -.1526$$

Figure 3.13 shows the block diagram for the system. The vehicle suspension block represents the dynamics of the quarter car model and this block outputs the current state values. The state values are then passed to the LQR controller which computes the desired damping force. The desired damping force along with the relative velocity as seen by the EMSA, $\dot{X}_1$, is passed to a reverse model of the EMSA to compute the desired input current. The current is sent to the EMSA and the actual damping force will

be generated and this process is repeated. Shown in Figure 3.14 is the block diagram for an active case. This model effectively takes out the EMSA. The states are passed to the LQR controller and the desired force is then computed directly and is sent back into the system. The passive system will simply have u(t) = 0 for all t.

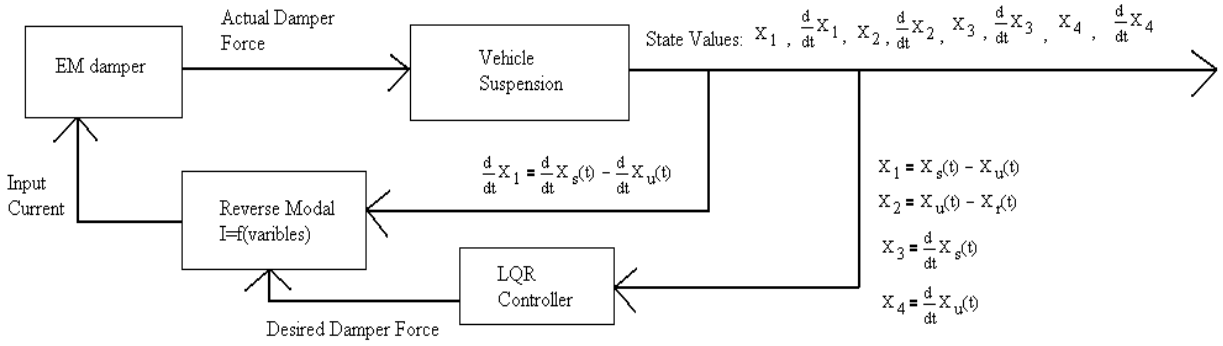

Figure 3.13: Block Diagram of Semi-Active System

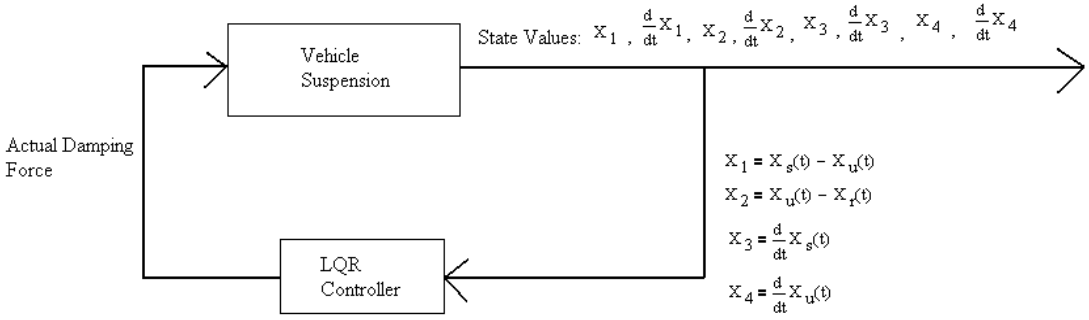

Figure 3.14: Block diagram for active suspension control

The force u(t) is found by:

$$u(t) = K \cdot X \tag{3.22}$$

Where K is a 1Xn vector consisting of gain values and X are the states. The gains are found by minimizing a cost function or what is commonly referred as a performance index. The cost function is determined by the designer and depends upon how much cost will be towards the input u(t) and the how much will be geared toward states [8]. The cost function has not yet been determined because the properties of the system need to be obtained prior to formulating the function.

Evaluation of Controller

The initial evaluation of the controller design will be done using Matlab-Simulink. To ensure that the system is modeled correctly, two separate Simulink files were created that are based upon [9]. The first model utilizes a built-in function block while the second model was created using individual blocks mimicking the built-in function block. Both of the Simulink models represent the same system except

that the second model allows for a road input. Shown in Figure 3.15 is the Simulink file with the built-in function block.

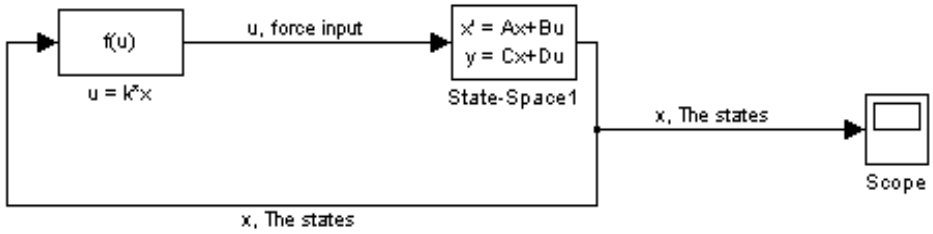

Figure 3.15: Simulink Model with built-in State-Space block

The state-space block represents Eqn. 3.20, neglecting the road input, with the matrices A and B being equal to what is shown in the state-space form. The block outputs y(t), in this case C is equal to an identity matrix and D is equal to zero, so that the output is y(t)=x(t). The input for the state-space block is u(t), which is equal to Eqn. 22. The values for the gains, k, were obtained by Ref. [6] as well as the mass, stiffness and damping values. This model does not allow a road profile input but still illustrates that the designed controller from [9] works appropriately, as shown in Figure 3.16, which is the output graph obtained from the scope block in the Simulink model.

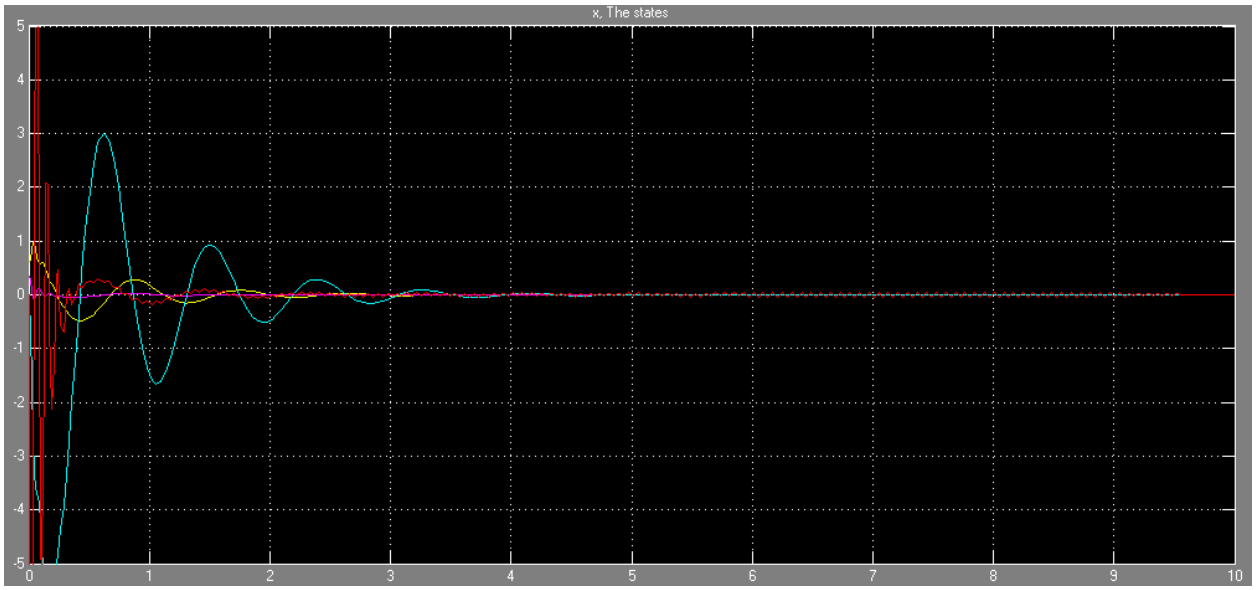

Figure 3.16: Output Plot of Initial Simulink Model

As of now, the magnitudes of the various states are irrelevant. Figure 3.16 simply illustrates that the controller forces the states to zero. The initial values of the states are multiplied by the gain values which may be large. That is why the magnitudes are initially large but decay within 4 seconds to zero.

The second model was created to evaluate the controller design, which needs a road input as well as other scopes, so as to monitor accelerations and/or other areas of interest. Initially, the same properties were used as in Figure 3.15, to ensure that the new model is correct. Shown in Figure 3.17 is the Simulink file that incorporates a road profile and exactly mimics the state space representation for the quarter car control model.

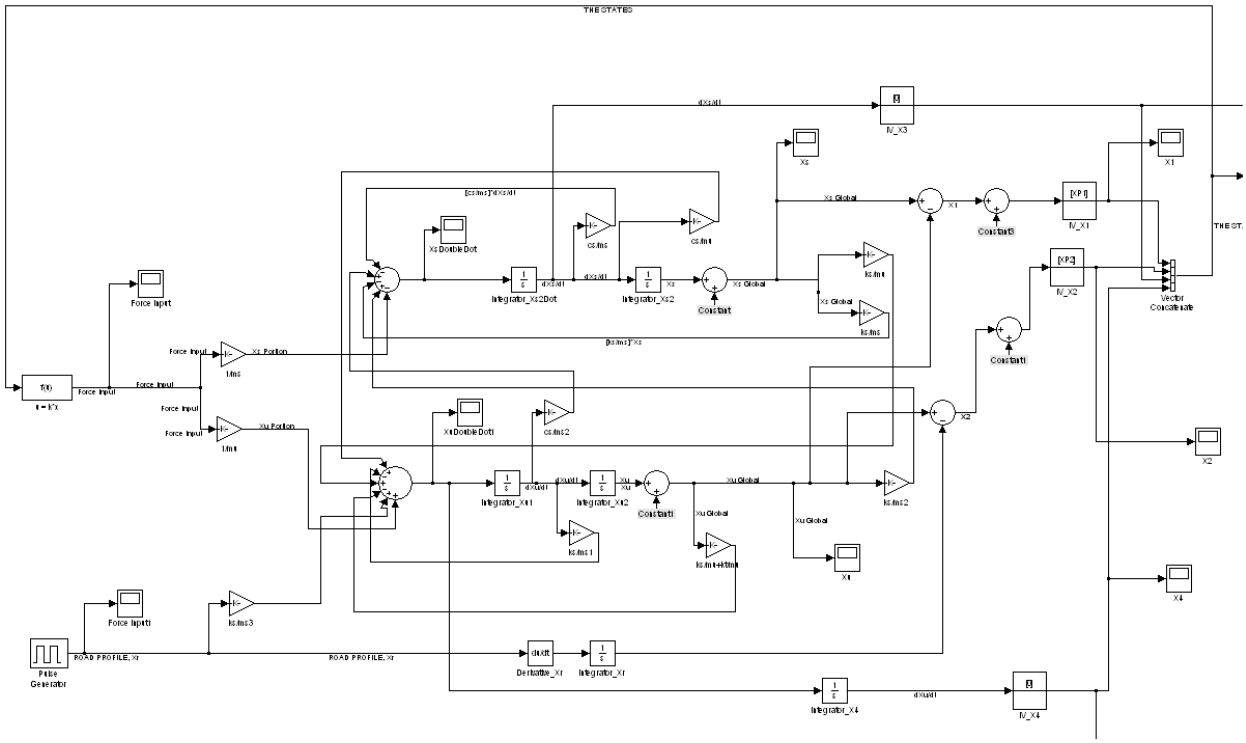

Figure 3.17: Simulink Model of ¼-Car with Control

The outputs of the states are almost exactly the same as the output for the first Simulink model. Figure 3.18 shows the output from the Figure 3.17 Simulink model. The major difference is that the yellow and purple lines are at a non-zero equilibrium. This is because they are the first two states which represent the difference of positions, so they should have a positive value.

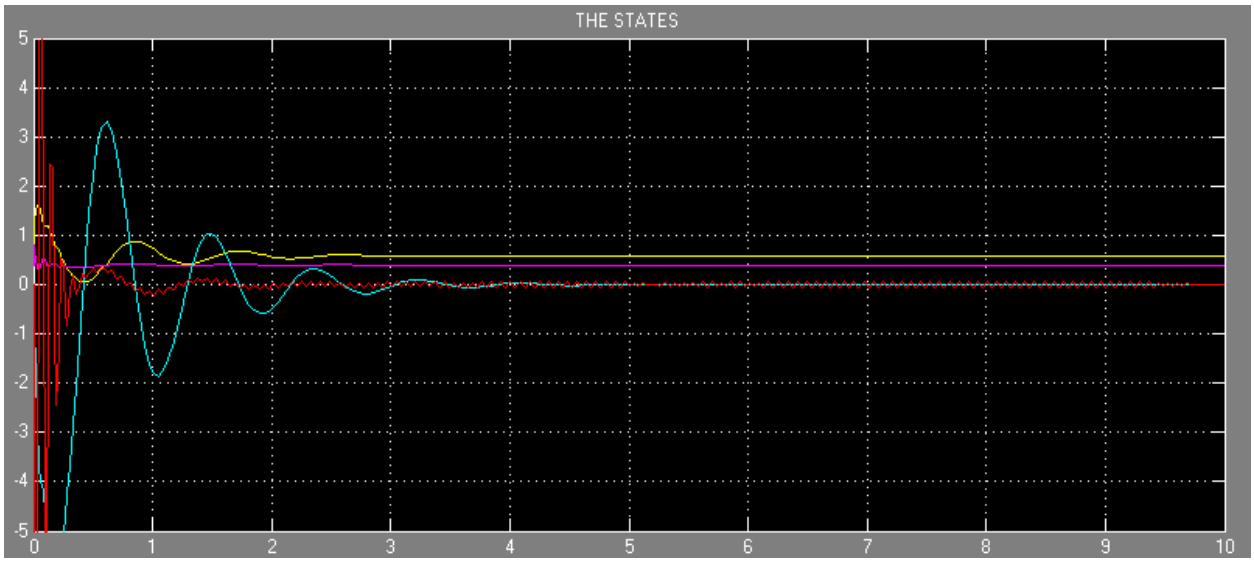

Figure 3.18: Output Plot of ¼-Car Simulink Model (Figure 3.17)

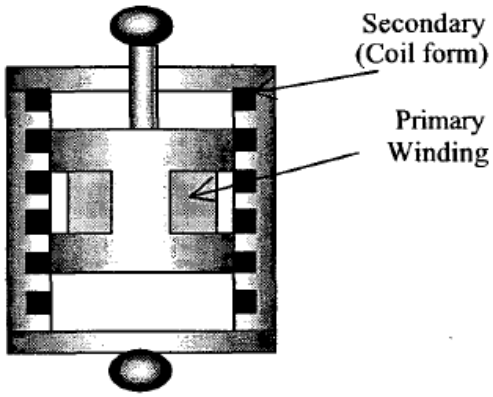

- **e_{coil} = Induced Voltage, coil form**
- **R_{coil} = Ohmic resistance, coil form**
- **f_d = Force opposing motion**
- **I_{coil} = Circulating current, coil form**
- **D = Damping coefficient**

Figure 3.19: Model of Electromagnetic Shock Absorber (Obtained from Ref. [6])

EMSA Model

The initial modeling of the EMSA will be done analytically. The current design is based upon Ref.[10]. Shown in Figure 3.19 is a schematic representation for the EMSA.

By moving the cylindrical coil form in the radial air-gap magnetic field an electric current is generated in the conducting material. And this current will produce a damping force opposing the motion of the coil form. The induced voltage in the coil form is:

$$\mathbf{e_{coil}} = 2\cdot\boldsymbol{\pi}\cdot\mathbf{a}\cdot\mathbf{B_a}\cdot\frac{\mathbf{d}}{\mathbf{dt}}\mathbf{X_1} \qquad (3.23)$$

Where a is the coil form radius, B_a is the radial air-gap magnetic field and $\dot{X}_1$ is the relative velocity as observed by the EMSA. In this case $\dot{X}_1$ is equal to the difference between $\dot{X}_s$ and $\dot{X}_u$. The Ohmic resistance of the coil form is:

$$\mathbf{R_{coil}} = \frac{2\cdot\pi\cdot a\cdot\rho}{h\cdot d} \tag{3.24}$$

Where ρ is the resistivity of the coil form material, h is the width of the coil form and d is the thickness of the coil form. The circulating current in the coil form obtained by dividing the induced voltage by the Ohmic resistance, neglecting the $\dot{X}_1$ in the induced voltage equation:

$$\mathbf{I_{coil}} = \frac{2\cdot\pi\cdot a\cdot B_a}{\frac{2\cdot\pi\cdot a\cdot\rho}{h\cdot d}} = \frac{B_a\cdot(h\cdot d)}{\rho} \tag{3.25}$$

The force generated opposing the motion of the coil form is:

$$\mathbf{F_d} = \left[2\cdot\pi\cdot a\cdot B_a\cdot\left(\frac{2\cdot\pi\cdot a\cdot B_a}{\frac{2\cdot\pi\cdot a\cdot\rho}{h\cdot d}}\right)\cdot\frac{d}{dt}X_1\right] = 2\cdot\pi\cdot a\cdot B_a\cdot I_{coil}\cdot\frac{d}{dt}X_1 \tag{3.26}$$

Notice that the term in the parentheses is equal to the circulating current in the coil form. The damping force of the EMSA is also equal to:

$$\mathbf{F_d} = C_u\cdot\frac{d}{dt}X_1 \tag{3.27}$$

Where C_u is the damping coefficient for the EMSA, C_u, can be obtained by equating eqn. 4a and eqn. 4b:

$$\mathbf{C_u} = \frac{2\cdot\pi\cdot a\cdot B_a^{\,2}\cdot h\cdot d}{\rho} = 2\cdot\pi\cdot a\cdot B_a\cdot I_{coil} \tag{3.28}$$

It is shown that by varying the induced voltage, the circulating current will change and consequently the damping coefficient will change. Therefore by increasing the induced DC voltage, the circulating current will increase and thus the damping coefficient and damping force will increase.

Simulation of the F800 Truck Model

The initial simulations of the F800 truck model will be performed in order to obtain mass and suspension properties of the vehicle. The values for the unsprung masses are already obtained by examining each component of the wheel/hub assembly and summing up the masses. Since the F800 is highly detailed, each wheel/hub assembly (front/rear passenger and driver sides) had to be examined. The total mass values will be obtained by placing four rigid walls under each wheel. By subtracting the unsprung masses from the total masses, the sprung masses will be obtained. This simulation is currently in-process;

however issues with the energy balance have postponed the results. Two more simulations will be needed to obtain the stiffness and damping properties of the F800 truck model.

Once the properties of the F800 truck are obtained through simulation via LS-Dyna, the performance index will then be evaluated, yielding gain values. The quality of these values will be evaluated using the Simulink model, and further adjustments will be made. Once satisfactory gain values are obtained, a sub-routine in LS-Dyna will be created to simulate the EMSA. The sub-routine will be based upon the block diagrams shown in Figure 3.13 and Figure 3.14. The three cases of suspension; passive, semi-active and active will be examined and compared.

3.2.3. References

1. http://en.wikipedia.org/wiki/Vehicle_dynamics
2. Chen, F. and Chen, S , "Assessment of vehicle safety behavior under adverse driving conditions." 11th American Conference on wind loading, San Juan, Puerto Rico, June 22-26, 2009.
3. Winkler, C. B. and Ervin, R. D., "Rollover of heavy commercial vehicles." UNTRI-99-19, The University of Michigan, Transportation Research , Michigan, August 1999.Institute.
4. Karnopp, D.; Crosby, M. J.; Harwood, R. A.; "Vibration Control Using Semi-Active Force Generators", ASME Journal, Vol.96, No. 2, 1974, pp. 619-626.Karnopp, D.; Crosby, M. J.; Harwood, R. A.; "Vibration Control Using Semi-Active Force Generators", ASME Journal, Vol.96, No. 2, 1974, pp. 619-626.
5. Poussot-Vassal, C.; Sename, O., Dugard, L., Gaspar, P., Szabo, Z., Bokor, J. "A New Semi-Active Suspension Control Strategy Through LVP Technique," Control Engineering Practice, Vol. 16, 2008, pp. 1519-1534.
6. Gupta, A.; Jendrzejczyk, J. A.; Mulcahy, T. M.; Hull, J. R.; "Design of Electromagnetic Shock Absorbers", International Journal of Mechanics and Materials in Design, Vol. 3, No. 3, 2007, pp. 285-291.
7. Du, H.; Sze, K.Y.; Lam, J.; "Semi-active H[infinity] control of vehicle suspension with magneto-rheological dampers", Journal of Sound and Vibration, Vol. 283, No. 3-5, 2005, pp. 981-996
8. Gordon, T.J., "Non-Linear Optimal Control of a Semi-Active Vehicle Suspension System", Chaos, Solutions And Fractals, Vol. 5, No. 9, 1995, pp. 1603-1617.
9. Gao, H.; Lam, J.; Wang, C.; "Multi-objective Control of Vehicle Active Suspension Systems Via Load-dependent Controllers," Journal of Sound and Vibration, Vol. 290, 2006, pp. 654-675.
10. Mirzaei, S.; Saghaiannejad, S.M.; Tahani, V.; Moallem, M.; , "Electromagnetic shock absorber," Electric Machines and Drives Conference, 2001. IEMDC 2001. IEEE International , vol., no., 2001, pp.760-764

3.3. Evaluating Soil Erosion

Introduction

TRACC has been working on riverbed scour (Steve Lottes) and bridge stability of bridges with piers in scour holes (Ron Kulak and Cezary Bojanowski) among other topics of interest to Turner-Fairbank Highway Research Center. Soil mechanics is important to both of the above problems. Traditional soil mechanics is applied to determining the adequacy of soil for supporting structures, for example bridge piers in scour holes. In addition, traditional soil mechanics is applicable to evaluating slope stability of scour holes. As a scour hole develops due to erosion it may reach an unstable configuration and part of the soil around the scour hole slumps into the scour hole. In contrast, soil erosion mechanics deals with the removal of soil from a surface.

On March 29-31, Kornel Kerenyi, Harold Bosch, and Jerry Shen—all from Turner Fairbank Highway Research Center—attended a CFD training course at TRACC. This provided the opportunity for TFHRC staff to interact with the TRACC staff: Steve Lottes, Cezary Bojanowski, and Ron Kulak. The topic of one of the meetings was the soil erosion experiment currently being conducted at TFHRC (http://www.fhwa.dot.gov/engineering/hydraulics/research/activities/current.cfm#). The experiment involves exposing the surface of soil to different flow conditions in a flume and measuring the rate of erosion. The test apparatus has both pressure and shear stress measuring capabilities. Figure 3.20 is a simplified illustration showing fluid flowing against a non-eroding horizontal surface that contains an opening in which soil is placed. As the shear stress from the flowing fluid erodes the top layer of soil, the soil is moved up to continue the experiment and determine erosion rates.

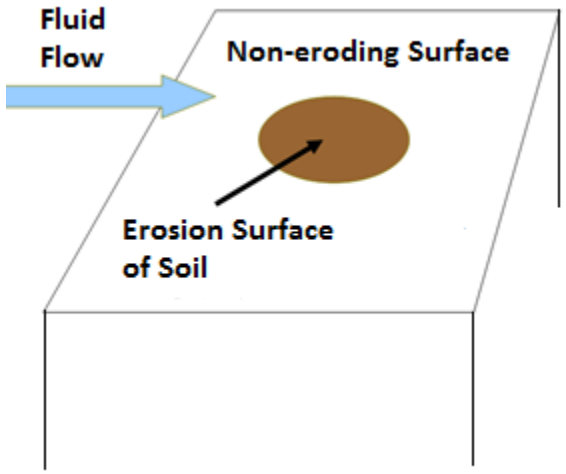

Figure 3.20: Simplified Illustration of TFHRC Ex-Situ Scour Test Device

It is accepted that the soil erosion rate is related to the shear stress applied by the flowing fluid over the soil surface. During our discussion, it was learned that the soil samples were not characterized, i.e., the failure surface of the soil sample was not known. The purpose of this Technical Note is to point out

standard laboratory tests that are used to characterize geomaterials for traditional civil engineering loading conditions. Some or all of these tests may need to be performed to characterize the soil during erosion. More thought needs to be given on the erosion aspect and this will be reported in the next Quarterly Report.

Soil Classification

The soil being tested in the TFHRC Ex-Situ Scour Test Device should be identified according to existing classification schemes. In the US there are two soil classification schemes: American Association of State Highway and Transportation Officials (AASHTO) and United Soil Classification System (USCS). The AASHTO system was developed for earthworks, embankments and roadbed materials. At the broadest level, the soils are classified as gravel, sand or silt, and clay.

Characterizing Test for Geomaterials

The standard test specimen for soil is a right circular cylinder (Figure 3.21). The test is performed by applying axial (σ_1) and lateral stresses (σ_2, σ_3) to the cylinder. The geometry of the cylinder is axisymmetric; so $\sigma_2 = \sigma_3$, which is called the lateral stress or confining stress/pressure (σ_c).

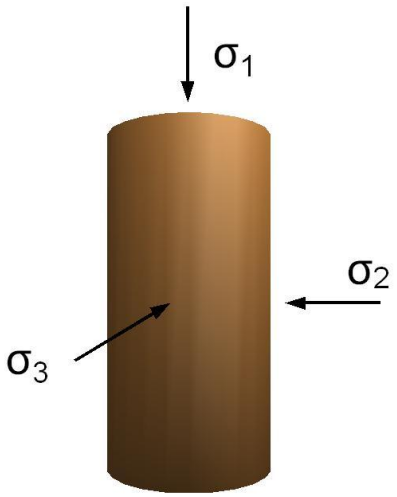

Figure 3.21: Standard Test Specimen for Soil Testing

Figure 3.22 shows a representative schematic for a triaxial testing apparatus. The soil sample is encased in a fluid-tight membrane and placed in a pressure vessel (Perspex cylinder) in the testing apparatus. The axial load (stress) is applied to the sample by the loading piston, and the confining pressure is applied to the cylinder by pressurizing the fluid (air) in the pressure vessel. The following tests are usually performed on soil samples to obtain material properties and the failure surface.

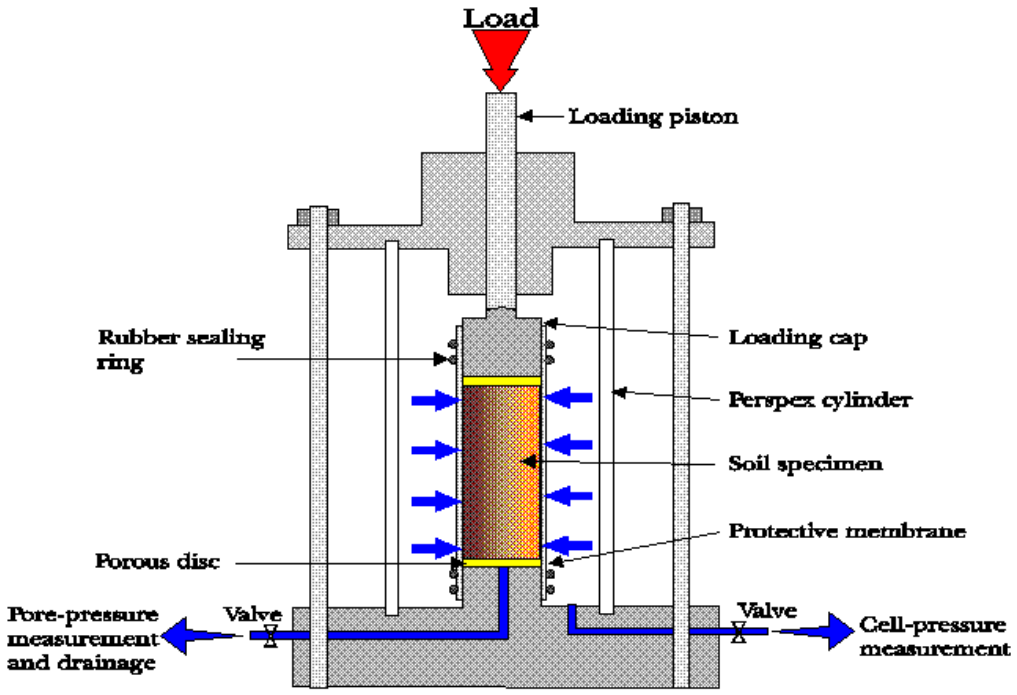

Figure 3.22: Triaxial Testing Appratus (http://www.geotechdata.info/geotest/triaxial-test)

The hydrostatic compression test is performed to determine the compaction behavior of soil. The test is performed by having all the stresses equal:

$$\sigma_1 = \sigma_2 = \sigma_3 \tag{3.29}$$

By definition, the pressure (mean stress) is given by:

$$p = (\sigma_1 + \sigma_2 + \sigma_3)/3 \tag{3.30}$$

The engineering volumetric strain is given by:

$$\varepsilon_v = \varepsilon_1 + \varepsilon_2 + \varepsilon_3 \tag{3.31}$$

Because LS-DYNA®/MPP is capable of treating problems in which large deformations occur, the required strain input is logarithmic volume strain, which is computed from the engineering volume strain by:

$$\ln\left(\frac{V}{V_0}\right) = \ln(1 - \varepsilon_v) \tag{3.32}$$

The above two equations are used to obtain the compaction response for soils. Characterizing the compaction response is important for predicting soil behavior during loading. To illustrate, Figure 3.23 shows the experimentally determined compaction response for Sandy Loam.

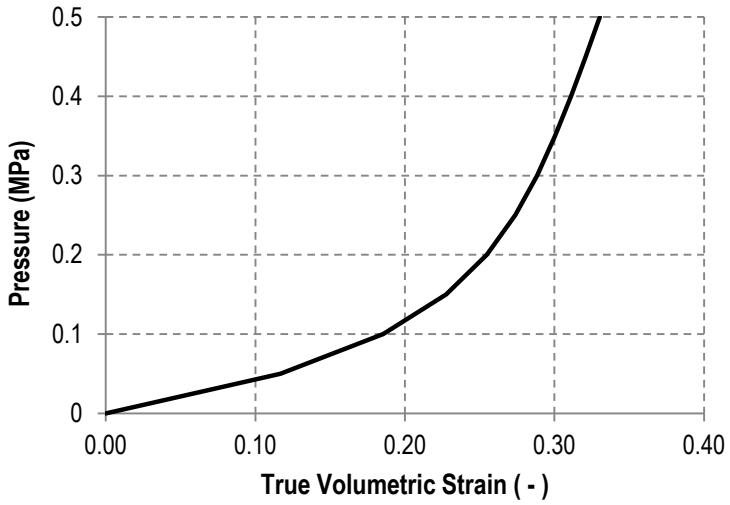

Figure 3.23: Triaxial hydrostatic compression data for Sandy Loam

Triaxial compression tests are used to define the strength envelope of the soil. Unlike the hydrostatic compression test, the axial and lateral stresses are not equal, and thus, the cylindrical test specimen experiences shear stress, which is equal to the difference between the principal stresses and is denoted either by SD or σ_Δ:

$$SD = \sigma_\Delta = \sigma_a - \sigma_c \tag{3.33}$$

In the triaxial compression test, the axial stress and lateral stress will be different. The test is performed by loading the specimen to a predetermined pressure under hydrostatic compression conditions. Next the lateral stress is held constant and the axial stress is increased until failure occurs. By performing the test over a range of confining pressures, the strength envelope for the soil is obtained. For illustrative purposes only, Figure 3.24 shows a typical failure envelope for soil showing the dependence on the mean stress (pressure). The points are data points obtained from three tests and the dashed line is the resulting fit to a shear failure model described below.

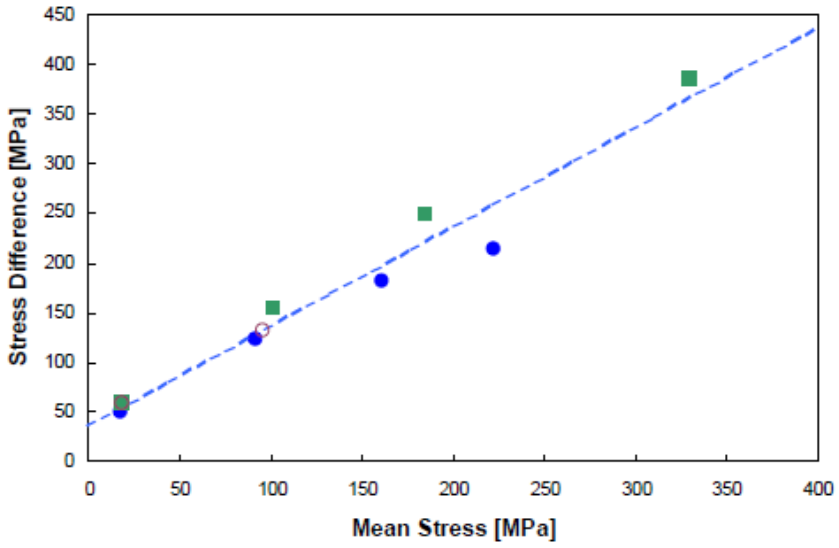

Figure 3.24: Typical Failure Envelop for Soil Obtained from Triaxial Compression Test Data

The triaxial extension test is performed in a similar manner. First, the specimen is loaded to a predetermined pressure under hydrostatic compression conditions, and then the axial stress is held constant and the lateral stress is increased.

The unconfined compression test is performed by having a zero lateral stress. This is the lowest estimate of the material strength.

For soils the uniaxial strain test is usually performed by placing the soil in a "rigid" cylinder to prevent lateral strain.

The uniaxial tension test is performed to determine the tensile failure response of soil, and the resulting response curve can be integrated to find the energy required to sever interparticle bonds on the failure plane.

Bulk density is a property of non-solid (particle) materials of which soil is one. It is not an intrinsic material property but depends on how the material is compacted. A core sample of soil is extracted and the soil is oven dried and weighed. For soils, bulk density is the mass of oven dried soil, m_s , divided by the core volume, V_c:

$$\rho_b = {}^{m_s}/_{V_c} \tag{3.34}$$

The water in soils is called porewater and it affects the strength of soils. The higher the water content the lower the soil strength. The water content of the soil being tested should be measured. Both the plastic limit and liquid limit of the soil should be obtained.

The void ratio is the ratio of the void space volume to the volume of solids and can be used to determine the porosity.

Failure Models for Soil

For traditional engineering applications, there are several failure models available that are applicable to soils. LS-DYNA has several models available for soils, and the simplest is the *Soil and Foam Model*. Here is a very terse description of the model. The deviatoric stress tensor is defined by:

$$s_{ij} = \sigma_{ij} + p\delta_{ij} \tag{3.35}$$

Where s_{ij} is the deviatoric stress tensor, σ_{ij} is the Cauchy stress tensor and δ_{ij} is the Kronecker delta. The second invariant, J_2', of the deviatoric stress tensor is given by:

$$J_2' = \frac{1}{2} s_{ij} s_{ij} \tag{3.36}$$

For the special case of triaxial compression, the second invariant is given by:

$$J_2' = \frac{{\sigma_\Delta}^2}{3} \tag{3.37}$$

The functional form of the shear failure surface is given as:

$$\sigma_\Delta = 3(a_0 + a_1 p + a_2 p^2) \tag{3.38}$$

The three constants (a_0, a_1, a_2) are fit to the experimental data.

The Drucker-Prager failure surface is the linear form of the shear failure surface (9), which is:

$$\sigma_\Delta = 3(a_0 + a_1 p) \tag{3.39}$$

This model is invoked when the constant a_2 is set to zero in the Soil and Foam Model.

Another failure criterion sometimes used to represent soils is the Mohr-Coulomb model, which is expressed as:

$$\tau = \sigma \tan(\phi) + c \tag{3.40}$$

where τ is the shear strength, σ is the normal stress, *c* is the cohesion, which is the intercept of the failure envelope with the τ axis, and φ is the slope of the failure envelope. Unfortunately, this model does not take into account the dependence on effective stress. Figure 3.25 shows the failure criteria in τ-σ space. Note the cohesion value can be obtained from the unconfined compression test.

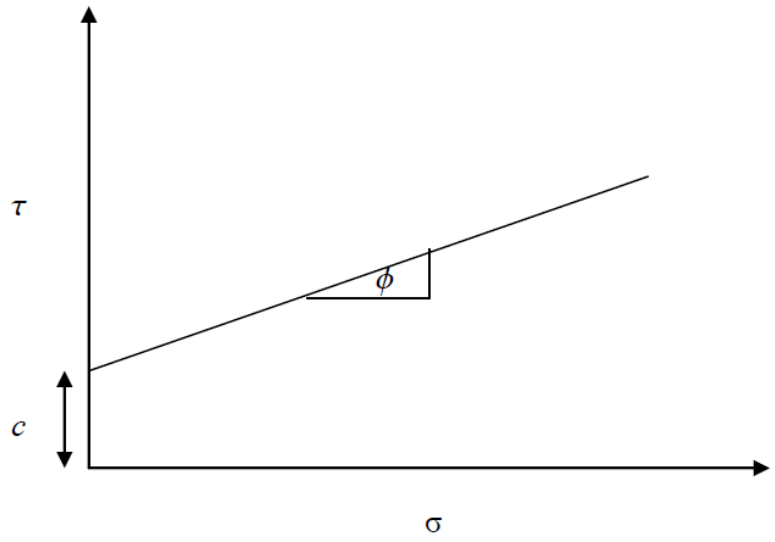

Figure 3.25: Mohr-Coulomb Failure Surface in τ-σ Space

The FHWA Soil Material Model available in LS-DYNA is Soil Material Model 147. The model treats isotropic materials with damage and is available for solid elements. The model is a modified Mohr-Coulomb surface to determine the pressure-dependent shear strength. It has parameters for modeling pore-water effects.

Summary

Riverbed scour and the stability of bridge piers in scour holes both involve aspects of soil mechanics. The stability problem relies on the traditional areas of soil mechanics, and the scour problem relies on traditional soil mechanics to model slope stability around the scour hole and soil erosion mechanics to model erosion.

Turner Fairbank Highway Research Center is performing erosion test on cohesive soils under different flow conditions. An Ex-Situ Scour Test Device has been developed and is being used to collect erosion data. It is generally accepted that erosion depends on the shear stress applied to the soil surface. Figure 5 above shows that the failure surface depends on both the soil compaction and shear stress. A highly compacted soil will fail at a higher stress than a lightly compacted soil. It is also known that water content will affect the strength of the soil. The higher the water content the lower the strength of the soil. The difference in strength can be an order of magnitude.

This report presents a terse overview of standard tests performed for characterizing soil. The tests are performed to (1) to determine parameters used in constitutive models and (2) to define the failure surface. The results of these tests are usually used for analysis of civil engineering structures with soil structure interaction based on a continuum mechanics approach.

With regard to the soil erosion problem, some tests may need to be performed to characterize the soil for the prediction of erodibility. If the strength of the soil being tested is the only item of interest, then the strength related tests are needed. On the other hand, if detailed modeling of the erosion process is

also of interest, then the test related to determining parameters for erosion rates also need to be performed. Other tests may need to be performed, and this will be determined as erosion mechanics is further researched.

Finally, TRACC will need more details on the Ex-Situ Scour Test Device and test results obtained to date.

Energy Systems Division
Argonne National Laboratory
9700 South Cass Avenue, Bldg. 362
Argonne, IL 60439-4815

www.anl.gov